HHS Public Access

Author manuscript

Cancer Res. Author manuscript; available in PMC 2024 July 16.

Published in final edited form as:

Cancer Res. 2024 January 16; 84(2): 226–240. doi:10.1158/0008-5472.CAN-23-1079.

SMALL CELL LUNG CANCER PLASTICITY ENABLES NFIB-INDEPENDENT METASTASIS

Julie H. Ko[1,2], **Kyle E. Lambert**[1,2], **Debadrita Bhattacharya**[1,2], **Myung Chang Lee**[1,2], **Caterina I. Colón**[1,2], **Haley Hauser**[1,2], **Julien Sage**[1,2,*]

[1]Department of Pediatrics, Stanford University, Stanford, CA 94305, USA

[2]Department of Genetics, Stanford University, Stanford, CA 94305, USA

Abstract

Metastasis is a major cause of morbidity and mortality in patients with cancer, highlighting the need to identify improved treatment and prevention strategies. Previous observations in pre-clinical models and tumors from patients with small cell lung cancer (SCLC), a fatal form of lung cancer with high metastatic potential, identified the transcription factor NFIB as a driver of tumor growth and metastasis. However, investigation into the requirement for NFIB activity for tumor growth and metastasis in relevant in vivo models is needed to establish NFIB as a therapeutic target. Here, using conditional gene knockout strategies in genetically engineered mouse models of SCLC, we found that upregulation of NFIB contributes to tumor progression, but NFIB is not required for metastasis. Molecular studies in NFIB wild-type and knockout tumors identified the pioneer transcription factors FOXA1/2 as candidate drivers of metastatic progression. Thus, while NFIB upregulation is a frequent event in SCLC during tumor progression, SCLC tumors can employ NFIB-independent mechanisms for metastasis, further highlighting the plasticity of these tumors.

Statement of significance—Small cell lung cancer cells overcome deficiency of the pro-metastatic oncogene NFIB to gain metastatic potential through various molecular mechanisms, which may represent targets to block progression of this fatal cancer type.

Introduction

Most cancer deaths result from the growth and spread of metastatic tumors, which impair organ function and disrupt physiological processes. Metastasis is a hallmark of cancer, but the mechanisms involved in this process are not fully understood. The difficulty in studying the metastatic process is in part due to its complexity: To metastasize, cancer cells employ a series of molecular programs that not only vary between different cancer types, but also between different contexts within a cancer type (1-3). Direct comparisons between metastases and their originating primary tumors are also often limited by the paucity of paired primary and metastatic tumor samples that can be obtained from patients (3,4).

*Corresponding Author and Lead Contact: Julien Sage, Stanford University, 265 Campus Drive, SIM1 G2078, Stanford, CA 94305-5457 – julsage@stanford.edu.

Declaration of Interests

J.S. has equity in, and is an advisor for, DISCO Pharmaceuticals. The other authors declare no competing interests.

Developing new therapies to treat metastatic disease requires a better understanding of both universal and cancer type-specific mechanisms underlying metastatic progression.

Small cell lung cancer (SCLC) is a highly metastatic carcinoma associated with over 200,000 deaths per year worldwide (5). Most patients already have widespread metastases at diagnosis, most commonly in the liver, brain, and bone (6). Patients with metastatic disease have a median survival of only ~1 year, and their tumors are rarely surgically resected (7,8). Study of SCLC metastasis is hindered by the limited number of models of SCLC progression. Surgical resection in SCLC is usually limited to early-stage patients without distant metastases, and xenografts derived from resected tumors often do not readily metastasize. Cell lines and xenografts derived from circulating tumor cells (CTCs) or metastatic tumors (9,10) also cannot easily model earlier steps of tumor progression, such as local invasion and intravasation.

Genetically engineered mouse models can address some of these limitations. The tumor suppressors *RB1* and *TP53* are inactivated in most human SCLC tumors (11), so conditional knockout mouse models of SCLC delete *Lox*-flanked alleles of *Rb1* (*Rb1*$^{f/f}$) and *Trp53* (*Trp53*$^{f/f}$) in lung epithelial cells *via* intratracheal instillation of adenoviral vectors expressing the Cre recombinase (12,13). Other alleles can be added to the *Rb1*$^{f/f}$;*Trp53*$^{f/f}$ *(RP)* mouse model to reflect the contributions of other recurrent alterations in human SCLC. Adding a conditional knockout of the *Rbl2* tumor suppressor gene to generate *Rb1*$^{f/f}$;*Trp53*$^{f/f}$;*Rbl2*$^{f/f}$ *(RPR2)* mutant mice accelerates tumor growth (14,15). Tumors in both *RP* and *RPR2* mutant mice are of the SCLC-A subtype, a predominant subtype of SCLC characterized by expression of the transcription factor ASCL1 (Achaete-Scute Family BHLH Transcription Factor 1) (16). The *Rb1*$^{f/f}$;*Trp53*$^{f/f}$;*H11*$^{CAG\text{-}LSL\text{-}MycT58A}$ *(RPM)* mouse model, with conditional expression of the *Myc*^{T58A} oncogene, generates tumors of the SCLC-N subtype, another common subtype of SCLC characterized by expression of the transcription factor NEUROD1 (17,18). In these SCLC mouse models, lung primary tumors eventually metastasize to distant organs, particularly the liver and lymph nodes, thereby providing models to investigate tumor progression *in vivo*.

In the *RPR2* model, initiating tumors with Cre recombinase driven by the ubiquitous CMV promoter results in early primary tumors that express low levels of the NFIB transcription factor. As tumors progress, cells upregulate *Nfib* expression through genomic amplification, expand as NFIB^{high} clonal populations, and seed metastases (19). NFIB levels are also elevated in late *RP* mutant mouse tumors and metastases, *RPM* mutant mouse tumors, and in a majority of human metastatic SCLC, where high levels of NFIB correlate with lower survival (18-23). Overexpression of NFIB at the time of *Rb1* and *Trp53* deletion results in tumors that are more metastatic than *RP* mutant tumors or *RP* mutant tumors overexpressing the MYCL oncogene (22). These data suggest a model in which upregulation of NFIB is sufficient to endow SCLC cells with a greater ability to metastasize. However, metastatic tumors with little to no NFIB expression have been observed in *RPR2* mutant mice given Ad-CGRP-Cre to specifically target pulmonary neuroendocrine cells (24), suggesting SCLC tumors are capable of metastasizing without NFIB in at least one context. While loss of NFIB methylation was recently shown to decrease metastases in the *RPR2* model (21), only one experimental approach thus far has tested the potential direct requirement for NFIB in

metastasis formation: In *RPR2* mutant mouse cell lines, knock-down of NFIB decreases the ability of these cells to form liver metastases upon tail vein injection (19).

Here we investigated the consequences of *Nfib* deletion in *RPR2* and *RPM* mutant mice. In these models, tumors with high NFIB expression show greater dependence on NFIB for growth, validating its role as an oncogenic factor in SCLC *in vivo*. Notably, while NFIB upregulation is a very frequent event in late tumors and metastases in the *RPR2* model, NFIB is not required for the development of metastases. Molecular analyses of the transcriptome and the chromatin state of NFIB wild-type and knockout SCLC cells in the *RPR2* model indicate that, when SCLC cells cannot use NFIB upregulation as a metastatic switch, they rely on other mechanisms such as the upregulation of transcriptional networks around ASCL1 and chromatin accessibility around FOXA1/2 binding to promote proliferation and metastasis.

Materials and Methods

Mouse models of SCLC

Mice were maintained according to practices prescribed by the National Institute of Health at Stanford's Research Animal Facility. Experiments with mice for this work were approved by the Institutional Animal Care and Use Committee (IACUC) at Stanford (APLAC protocol #13565). Additional accreditation of Stanford Research Animal Facility was provided by the Association for Assessment and Accreditation of Laboratory Animal Care.

The $Rb1^{flox/flox};Trp53^{flox/flox};Rbl2^{flox/flox}$ *(RPR2,* or *TKO)* mouse model and the $Rosa26^{mTmG}$ *(*$R26^{mTmG}$) allele have been previously described (15,19). *RPM* mice were provided by Trudy Oliver (18). $Nfib^{flox/flox}$ (*Nfib*$^{f/f}$ thereafter) mice were provided by Richard Gronostajski (25). Mice were maintained in a mixed C57BL6;129SVJ background.

Nfib^{f} mice were crossed to *RPR2;*$R26^{mTmG}$ mice to generate *RPR2;*$R26^{mTmG}$*;Nfib*$^{f/+}$ mice, which were then crossed to each other to generate *RPR2;*$R26^{mTmG}$*;Nfib*$^{f/f}$ mice and *RPR2;*$R26^{mTmG}$*;Nfib*$^{+/+}$ littermate controls. *Nfib*^{f} mice were similarly crossed to *RPM* mice to generate *RPM;Nfib*$^{f/f}$ mice and *RPM;Nfib*$^{+/+}$ littermate controls.

Tumors were initiated at 8-12 weeks of age with intratracheal instillation of Adeno-CMV-Cre (Baylor College of Medicine, Houston, TX) or Adeno-CGRP-Cre (University of Iowa). *RPR2* mice were given $4x10^7$ plaque-forming units (pfu) of Adeno-CMV-Cre or $4x10^8$ pfu of Adeno-CGRP-Cre. *RPM* mice were given $1x10^8$ pfu of Adeno-CGRP-Cre. Animals were euthanized and tumors were collected at set time points post-initiation or when they showed signs of respiratory distress. Mice were housed at 22°C ambient temperature with 40% humidity and a light/dark cycle of 12 hours (7am – 7pm). Mice of both sexes were used in the experiments in approximately equal numbers.

Histology and immunostaining

Lung and liver lobes were fixed for 48 hours in 10% neutral buffered formalin before paraffin embedding. Paraffin sections were deparaffinized with Histo-Clear (National Diagnostics HS-200) and gradually rehydrated from ethanol to water. Antigen retrieval

was carried out in citrate-based unmasking solution (Vector Laboratories H-3300) by microwaving at full power until boiling, then 30% power for 15 min, then left to cool at room temperature for 10 min before washing with water. Endogenous peroxidase was blocked by incubating slides in 3% hydrogen peroxide for 1 h. Sections were washed in PBST (PBS with 0.1% Tween-20) and blocked in 5% horse serum for 1 h. For immunostaining with anti-ASCL1 antibodies, endogenous mouse IgG were blocked by washing sections in PBST, incubating with Goat F(ab) Anti-Mouse IgG H&L (ab6668) diluted in PBS for 1 h, then washing in PBST for 30 min. All sections were incubated with primary antibody diluted in PBST overnight at 4°C.

For immunohistochemistry, sections (except those with anti-HES1 antibodies) were developed using ImmPRESS®HRP Horse Anti-Rabbit IgG Polymer Detection Kit (Vector Laboratories MP-7401) following the manufacturer's protocol. Sections with anti-HES1 were developed using ImmPRESS® Excel Amplified Polymer Staining Anti-Rabbit IgG Peroxidase Kit (Vector Laboratories MP-7601) following the manufacturer's protocol. All sections used DAB substrate kit (Vector Laboratories SK-4100) for color development. Sections were counterstained with hematoxylin (Sigma-Aldrich HHS32-1L), gradually dehydrated from water to ethanol to xylene, and mounted with Refrax mounting medium (Anatech Ltd711). Primary antibodies were used at the following dilutions: anti-ASCL1 (D-7, Santa Cruz sc-374104, 1:100), anti-CDH1 (E-Cadherin 24E10, CST 3195S, 1:500), anti-GFP (D5.1, CST 2956S, 1:100), anti-HES1 (D6P2U, CST 11988S, 1:200), anti-Ki-67 (SP6, ThermoFisher RM9106-S0, 1:200), anti-NFIB (Abcam ab186738, 1:2000), anti-UCHL1 (Sigma-Aldrich HPA005993, 1:2500). Research resource identifiers (RRIDs) for antibodies are listed in Table S1.

Tumor and immunostaining quantification

Sections were imaged using Keyence BZ-X700 all-in-one fluorescence microscope with BZ-X Viewer program version 1.3.1.1. Quantified sections were imaged at low magnification and stitched together with BZ-X Analyzer 1.4.0.1. Image analysis was conducted with Fiji 1.53t.

Stitched images were deconvolved using the color deconvolution plugin bundled with Fiji (26). Tumors were manually traced on each deconvolved hematoxylin image and saved as ROIs (regions of interest) in Fiji. At the 4.5-month timepoint, we used GFP expression from the $R26^{mTmG}$ allele on serial sections to identify the ROIs that were tumors and filter out inflammation before quantifying tumor number, tumor burden, or immunostaining.

Tumor area and immunostaining signal were measured by thresholding deconvolved images and measuring only within the tumor regions. Tumor areas were quantified in deconvolved eosin images at a single threshold. H-scores for immunostaining signal were quantified as 3 x % tumor area with high staining intensity + 2 x % tumor area with medium intensity + 1 x % tumor area with weak intensity. The % tumor area with each staining intensity was measured in deconvolved DAB images by setting three different thresholds.

Cell culture

Cell lines were cultured in DMEM (Hyclone SH30243.01) supplemented with 10% bovine growth serum (Hyclone SH3054103HI) and penicillin-streptomycin-glutamine (Gibco 10378016) at 37°C in standard cell culture incubators. All cells were routinely tested (MycoAlert Detection Kit, Lonza) and confirmed to be free of mycoplasma contamination. N2N1G and 12N1G murine SCLC cell lines have been described previously (19).

AlamarBlue cell proliferation assay

Cells were seeded at 8,000 cells per well in a 96-well plate in triplicate with four time points, and AlamarBlue reagent was added to a new time point every two days (with the day 0 timepoint starting immediately after seeding). Plates were incubated at 37°C for two hours after reagent addition, then read using a plate reader.

Cell line generation

Individual tumors (up to ~5 mm in diameter, or a smaller piece from the edge of a large tumor to avoid necrotic cores) were dissected from lungs or livers of *RPR2* or *RPR2;Nfib*$^{f/f}$ mutant mice. Tumors or tumor pieces were finely chopped with a razor blade and digested for 15 min at 37°C in 3 mL of L-15 medium (Sigma L1518) containing 4.25 mg/mL Collagenase I (Sigma C0130), 1.4 mg/mL Collagenase II (Sigma 6885), 4.25 mg/mL Collagenase IV (Sigma 5138), 0.625 mg/mL Elastase (Worthington LS002292), and 0.625 mg/mL DNase I (Roche 10104159). The digested mixture was filtered through a 40 μm filter and centrifuged at 400 g for 5 min at room temp, and the resulting pellet was resuspended in 500 μL RBC lysis buffer (eBioscience 00-4333-57) for 30 sec, diluted in 10 mL PBS, and centrifuged at 400 g for 5 min at room temp. The pelleted cells were then resuspended in 1.5 mL cell culture media (DMEM with 10% BGS and 1X PSQ) and plated in a single well of a 12-well plate. Tumor cells were left alone until they showed visible signs of growth by forming tight spherical aggregates typical of most murine SCLC cell lines or proliferating as adherent cells. All cell lines grew as spherical aggregates or as a mix of spherical aggregates and adherent cells.

SCLC CellMiner Cross Database

The heatmap of mRNA expression (log2) of *MYC* and mRNA expression (log2) of *NFIB* from the SCLC NCI-DTP cell line set was obtained using the SCLC-CellMinerCDB online tool (v1.2) (27).

RNA-seq analysis

Individual tumors were dissected from the lungs and livers of *RPR2* or *RPR2;Nfib*$^{f/f}$ mutant mice at morbidity, snap-frozen, and sent to Azenta Life Sciences for RNA extraction and sequencing. Samples are listed in Table S1. Total RNA isolation, polyA selection, quality control, library preparation, and sequencing were performed by Azenta using Illumina HiSeq platform (2 x 150bp, ~350M paired-end reads). Transcript quantification was conducted with Salmon (v0.12.0) (28) with mouse genome version GRCm38. DESeq2 (v1.34.0) was used to calculate differential expression (29) (Supplementary Data 1).

Gene set enrichment analysis (30,31) was performed through the GSEAPreranked module (v7.3.4) on GenePattern (32). From the default parameters, permutation type was changed to gene_set, and the metric for ranking genes was changed to log2_Ratio_of_Classes. GSEA was performed on pre-ranked lists of genes that were differentially expressed between metastatic and primary tumors with an adjusted p value < 0.05. The gene set is a custom list of genes classically associated with axonogenesis and axon guidance, as described in (33).

Enriched terms and cell types were identified from the KEGG 2021 Human pathway and the Mouse Gene Atlas in differentially expressed genes using Enrichr (34-36). For the KEGG 2021 Human enrichment, differentially expressed genes were first filtered for those that were not listed as liver genes in the Mouse Gene Atlas.

Low-pass whole genome sequencing analysis

Genomic DNA was extracted from *RPR2* and *RPR2;Nfib*$^{f/f}$ cell lines using the AllPrep DNA/RNA Mini Kit (Qiagen 80204) following the manufacturer's protocol. The library was prepared using the Illumina DNA Prep, (M) Tagmentation kit (Illumina 20018704, formerly Nextera DNA Flex) and IDT for Illumina DNA/RNA UD Indexes Set B (Illumina 20027214, formerly IDT for Illumina Nextera DNA Unique Dual Indexes Sets B) following the manufacturer's protocol. Individual libraries were sent to Novogene for quality control, pooling, and sequencing on a partial NovaSeq 6000 lane (PE150) at 0.8X coverage. Reads were trimmed of adapters using Trimmomatic (v.0.39) (37), aligned to the mm39 genome using BWA-MEM (v.0.7.17) (38), and PCR duplicates removed using Picard's MarkDuplicates (v.2.26.10). The resulting BAM files were used to call copy number variation using CNVkit (v.0.9.9) (39).

ATAC-Seq library preparation and sequencing

To perform ATAC-seq with mouse SCLC cell lines, ~100,000 suspension cells per cell line were collected, trypsinized, and processed using the OMNI-ATAC-Seq protocol (40). Briefly, cells were washed with 1 ml of ice-cold ATAC-RSB buffer and centrifuged at 500rcf for 5 minutes at 4°C. Next, the pellets were resuspended in 100µl of chilled ATAC-RSB-LYSIS and incubated on ice for 3 minutes. Lysis was stopped by adding 1mL of ATAC-RSB-WASH to each sample, which were again centrifuged for 5 minutes at 500rcf. The supernatant was removed, and the pellet was resuspended in 50µl of OMNI-ATAC Mix and incubated in a mixing (500rpm) thermoblock at 37°C for one hour. Tagmented DNA was purified using a Qiagen MinElute Kit (#28204), with 21µl of elution buffer warmed to 55°C. Library amplification PCR was performed with the NEBNext Ultra II Q5 2X Master Mix (NEB #M0544S) using Nextera primers for 12 cycles. DNA concentration was measured using a Qubit DNA HS Assay (ThermoFisher #Q33230). Individual samples were pooled sequenced on an Illumina NextSeq500 using the 75bp kit in a paired end configuration.

ATAC-Seq sequence processing

Raw sequencing reads were demultiplexed and trimmed using CutAdapt (v2.10) in paired-end mode with the forward and reverse Nextera sequencing adapters (Fwd – CTGTCTCTTATACACATCT, Rev- AGATGTGTATAAGAGACAG) and a minimum read

length of at least 25. Next, Bowtie2 (41) was used to align paired-end reads to the ENSEMBL mm10 genome (GRCm38), with the following settings: "--local --very-sensitive-local --no-unal --no-mixed --no-discordant". PicardTools (https://github.com/broadinstitute/picard) was used to mark duplicates, which were then filtered from the BAM files using samtools (42). MACS2 was used to call peaks genome-wide, with a q value of 0.05 and the arguments "-f BAMPE -g $GENOME_SIZE --nomodel --shift 37 --extsize 73" (43). Downstream analysis, including generation of consensus peakset and determining differential peaks between conditions, was performed using DiffBind (44). Motif enrichment analysis was performed using HOMER.

CUT&RUN library preparation, sequencing, and analysis

CUT&RUN was performed using on mouse SCLC cell lines using the CUTANA ChIC/CUT&RUN Kit (EpiCypher 14-1048) and the CUTANA CUT&RUN Library Prep Kit (EpiCypher 14-1001) according to the manufacturer's protocols. FOXA1 binding was detected using anti-FOXA1 (Abcam, ab170933). Libraries were sequenced by an Illumina NovaSeq PE150 (100G) platform, with ~20M paired reads per sample.

The demultiplexed CUT&RUN sequencing reads underwent preprocessing steps as follows: In paired-end mode, CutAdapt (v2.10) was used to trim sequences. Trimming involved the removal of TruSeq sequencing adapters from both the forward (5'-AGATCGGAAGAGCACACGTCTGAACTCCAGTCA-3') and reverse (5'-AGATCGGAAGAGCGTCGTGTAGGGAAAGAGTGT-3') ends, and reads were retained only if they met a minimum length threshold of 25 bases. Subsequently, alignment to the ENSEMBL mm10 genome was performed using Bowtie2 (41) with specific options, including '–local –very-sensitive-local –no-unal –no-mixed –no-discordant,' and alignments exceeding 1000 base pairs were excluded. To identify duplicate reads, PicardTool (https://github.com/broadinstitute/picard) was utilized, followed by the removal of duplicates from the BAM files using samtools. Genome-wide peak calling was conducted using MACS2, employing a significance threshold (q value) of 0.05, along with the arguments '-f BAMPE -g $GENOME_SIZE -q 0.05 –call-summits.' Subsequent analyses, such as motif enrichment, generation of peak profiles, and quantification of FOXA1 binding, were performed using Homer, Deeptools (45), and the DiffBind (44) packages, respectively.

Quantitative immunoassay

Cells were lysed in RIPA buffer (Thermo Fisher Scientific 89900) supplemented with protease and phosphatase inhibitors (Roche cOmplete ULTRA tablets, Mini, EASYpack 05892970001 and PhosSTOP EASYpack 04906845001). Protein concentration was measured using the Pierce BCA Protein Assay Kit (ThermoFisher #23227). 1 μg of protein was analyzed using the capillary-based Simple Western assay on the Wes system (ProteinSimple) and the Compass software v4.0.0 (ProteinSimple), according to the manufacturer's protocol. Anti-NFIB (Abcam ab186738, 1:10000) and anti-FOXA1 (Abcam ab170933, 1:5000) were run simultaneously with anti-HSP90 (CST 4874S, 1:5000) as a loading control.

Statistics and reproducibility

Statistical significance was assayed with GraphPad Prism software. The specific tests used are indicated in the figure legends. Data are presented as mean ± standard deviation or mean ± standard error as indicated in the figure legends. Mice were randomized where applicable, and quantifications from *in vivo* experiments were performed in at least two biological replicates as indicated in the figure legends. Two liver tumors (1548-liver from *RPR2* and 997-liver from *RPR2;Nfib*$^{f/f}$) were excluded from the RNA-sequencing data because they were determined to not be SCLC: They had low expression of all SCLC markers by RNA-sequencing, and liver sections from the same mice showed presence of metastases that did not resemble SCLC by histology. Investigators were not blinded to allocation during experiments and outcome assessment.

Data availability

RNA sequencing, ATAC sequencing, and CUT&RUN datasets generated in this study are available at Gene Expression Omnibus (GEO) under Super Series GSE228334 [https://www.ncbi.nlm.nih.gov/geo/query/acc.cgi?acc=GSE228334]. Whole genome sequencing datasets are available at the NCBI Sequence Read Archive (SRA) under accession PRJNA945077 [https://www.ncbi.nlm.nih.gov/sra/PRJNA945077]. The code for the whole genome sequencing, RNA sequencing, ATAC sequencing, and CUT&RUN analyses are available at Zenodo, DOI: 10.5281/zenodo.7878261. mRNA expression (log2) from the SCLC NCI-DTP cell line set is publicly available through the SCLC-CellMinerCDB online tool (v1.2) (27). All other raw data are available upon request from the corresponding author.

Results

NFIB is not required for cancer initiation in the RPR2 mouse model of SCLC-A

To investigate the role of NFIB in SCLC tumor development *in vivo*, we crossed conditional *Nfib* knockout mice (*Nfib*$^{f/f}$ mice) to the *RPR2* mouse model of SCLC with the *Rosa26*$^{mTmG/mTmG}$ (*R26*^{mTmG}) fluorescent reporter allele (hereafter, *RPR2* mice) to generate *Rb1*$^{f/f}$;*Trp53*$^{f/f}$;*Rbl2*$^{f/f}$;*R26*^{mTmG};*Nfib*$^{f/f}$ mice (hereafter, *RPR2;Nfib*$^{f/f}$ mice). In these *RPR2;Nfib*$^{f/f}$ mutant mice, *Nfib* is knocked out at tumor initiation by concurrent deletion of *Nfib* along with the *Rb1*, *Trp53*, and *Rbl2* tumor suppressor genes by Ad-CMV-Cre. Cells expressing Cre also switch from tdTomato-positive to GFP-positive (19), and in this model, tumors can be identified by histology and by immunostaining for GFP (Fig. 1A) (see Methods).

NFIB is required for lung development in mice (25) and is expressed in early primary *RPR2* mutant tumors (before *Nfib* gene amplification) (19). This raised the possibility that NFIB is required for tumor initiation and development in this mouse model. We compared primary lung tumors in *RPR2* and *RPR2;Nfib*$^{f/f}$ mutant mice 4.5 months after Ad-CMV-Cre infection, at a time when primary tumors are relatively small. We found that both the number of detectable lesions and total tumor burden in the lungs of *RPR2;Nfib*$^{f/f}$ mutant mice were not significantly different compared to *RPR2* mutant controls (Fig. 1B-D). Immunostaining for NFIB confirmed that all *RPR2;Nfib*$^{f/f}$ mutant tumors had lost expression of NFIB (Fig. 1E,F), showing efficient recombination of the *Nfib*$^{f/f}$ alleles and suggesting little to no

selection pressure to retain NFIB in early stages of tumor development in this mouse model when NFIB levels are low.

Loss of NFIB in *RPR2;Nfib*$^{f/f}$ mutant tumors may also lead to changes in cell fate, but we found that the tumors in *RPR2;Nfib*$^{f/f}$ mutant mice histologically resembled tumors in *RPR2* mutant mice. Immunostaining for ASCL1, a key marker of the SCLC-A subtype, showed no difference between *RPR2* and *RPR2;Nfib*$^{f/f}$ mutant lung tumors (Fig. 1G,H). In addition, there was no significant difference in the expression of the proliferation marker Ki67 between *RPR2* and *RPR2;Nfib*$^{f/f}$ mutant lung tumors (Fig. 1I,J). *RPR2* mutant tumors initiated by Ad-CMV-Cre are comprised of neuroendocrine and less/non-neuroendocrine cancer cells (46,47), and immunostaining for the neuroendocrine marker UCHL1 and the non-neuroendocrine marker HES1 showed no difference in heterogeneity between *RPR2* and *RPR2;Nfib*$^{f/f}$ mutant lung tumors (Fig. 1K,L).

Together, these experiments indicate that NFIB is not required for the initiation and the early development of SCLC-A tumors in the *RPR2* mouse model.

NFIB promotes tumor progression when upregulated in the RPR2 mouse model of SCLC-A but is not required for metastasis

To determine if loss of NFIB affected late tumor progression in the *RPR2* model, we compared tumor development in mutant mice 6.5 months after initiation, when some *RPR2* mutant tumors usually have gained metastatic potential. At this time point, we observed a significant reduction in tumor burden in the lungs of *RPR2;Nfib*$^{f/f}$ mutant mice compared to *RPR2* mutant mice (Fig. 2A,B). As expected for this time point (19), *RPR2* mutant tumors showed a wide range of NFIB expression, indicating that some clonal populations in the tumors have upregulated NFIB expression. In contrast, nearly all *RPR2;Nfib*$^{f/f}$ mutant tumors remained negative for NFIB expression with very rare exceptions (Fig. S1A,B). Immunostaining for Ki67 showed an association between higher NFIB expression and increased proliferation in *RPR2* mutant tumors (Fig. S1C-E). This difference in proliferation is likely contributing to the difference in tumor burden between *RPR2;Nfib*$^{f//f}$ and *RPR2* mutant mice. In cell lines derived from *RPR2* and *RPR2;Nfib*$^{f/f}$ tumors, there was a trend for cell lines with high expression of NFIB to proliferate faster than cell lines with no NFIB expression (Fig. S1F,G). Furthermore, mice in the *RPR2* model generally die from their lung tumor burden. Accordingly, when we aged *RPR2* and *RPR2;Nfib*$^{f/f}$ mutant mice until moribund, we found that *RPR2;Nfib*$^{f/f}$ mutant mice lived significantly longer than *RPR2* mutant mice (Fig. 2C). *RPR2;Nfib*$^{f/f}$ mutant tumors expressed no detectable NFIB at that time by immunostaining (Fig. S1H).

The difference in tumor growth at later stages of SCLC development in *RPR2* and *RPR2;Nfib*$^{f/f}$ mutant mice made it more challenging to comparatively assess the seeding of metastases between NFIB wild-type and knockout tumors, as fewer metastases would be expected to be seeded in mice with lower tumor burdens. However, tumor burden and tumor histology at death in *RPR2* and *RPR2;Nfib*$^{f/f}$ mutant mice were similar between the two genotypes (Fig. 2D-E and Fig. S1I), allowing us to compare metastases while controlling for primary tumor size, with the limitation that metastases had on average more time to develop in *RPR2;Nfib*$^{f/f}$ mutant mice. At death, 76% of *RPR2* mutant mice (n=21) and 50%

of *RPR2;Nfib*$^{f/f}$ mutant mice (n=14) had liver metastases (Fig. 2F). Metastatic tumor burden by area and by number were similar at this time point (Fig. 2G,H). None of the *RPR2;Nfib*$^{f/f}$ mutant liver metastases expressed detectable levels of NFIB by immunostaining (Fig. 2I) but were still histologically similar to *RPR2* mutant liver metastases, with similarly high ASCL1 immunostaining and little to no HES1 immunostaining (Fig. 2J and Fig. S1J).

Thus, tumor growth in the *RPR2* model is more dependent on NFIB as NFIB levels increase during tumor progression, but tumors in *RPR2;Nfib*$^{f/f}$ mutant mice are still metastatic and can still form liver metastases without NFIB.

NFIB is not required for tumor development or metastasis in RPR2 tumors initiated in pulmonary neuroendocrine cells

To test if NFIB is necessary for tumor progression and metastasis in SCLC tumors originating from pulmonary neuroendocrine cells (PNECs), we infected *RPR2* and *RPR2;Nfib*$^{f/f}$ mice with Ad-CGRP-Cre. At morbidity, we found that both Ad-CGRP-Cre *RPR2* and *RPR2;Nfib*$^{f/f}$ mutant lungs had similar tumor burden (Fig. S2A,B). Because of the lower number of primary tumors compared to Ad-CMV-Cre (24), Ad-CGRP-Cre *RPR2* and *RPR2;Nfib*$^{f/f}$ mutant mice were less likely to die from lung tumor burden and frequently died from other health issues, and their survival times were similar (Fig. S2C). Primary lung tumors in *RPR2;Nfib*$^{f/f}$ mutant mice given Ad-CGRP-Cre were almost all NFIB^{neg} (Fig. S2D,E), and all *RPR2;Nfib*$^{f/f}$ mutant mice harvested at morbidity had NFIB^{neg} liver metastases (Fig. S2F-H). We note that in this analysis, *RPR2* mutant mice had a greater proportion of NFIB^{high} tumors than previously reported (24), possibly due to differences in genetic backgrounds. Two of the *RPR2;Nfib*$^{f/f}$ mutant mice had lung tumors and liver metastases with low but detectable levels of NFIB (Fig. S2G,H), but these tumors were the exception and may come from the few primary tumors with no deletion of *Nfib* (Fig. S2E).

Overall, our findings show that in the *RPR2* model, NFIB is not required for tumor initiation or metastasis in tumors initiated from PNECs.

NFIB is required for cancer development in a mouse model of SCLC-N with high levels of NFIB at initiation

Our current work and other previous studies have focused on the role of NFIB in mouse models of SCLC-A (19,21-23), and whether NFIB contributes to tumor growth and metastasis in other SCLC subtypes remains unknown. The *Rb1*$^{f/f}$*;Trp53*$^{f/f}$*;H11*$^{CAG\text{-}LSL\text{-}MycT58A}$ *(RPM)* mouse model of SCLC is characterized by high levels of the NEUROD1 transcription factor and is thus a relevant model for the SCLC-N subtype (16,18). Notably, *RPM* mutant tumors express high levels of NFIB from the time they are initiated, which is likely a consequence of the direct transcriptional activation of *Nfib* by MYC in this model (18).

To investigate whether NFIB is necessary for tumor development in the *RPM* model, we crossed *Nfib*$^{f/f}$ mutant mice to *RPM* mice to generate *RPM;Nfib*$^{f/f}$ mutant mice. Around 30 days after tumor initiation with Ad-CGRP-Cre, when tumors in the *RPM* model are readily visible, we observed a trend for fewer tumors in lung sections from *RPM;Nfib*$^{f/f}$ mutant mice compared to *RPM* controls (Fig. 3A,B). However, unlike in *RPR2;Nfib*$^{f/f}$ mutant mice,

in which nearly all tumors efficiently knocked out *Nfib*, most *RPM;Nfib*$^{f/f}$ mutant tumors retained similarly mid/high levels of NFIB as in control *RPM* tumors (Fig. 3C,D). The large number of NFIB^{high} tumors in *RPM;Nfib*$^{f/f}$ lungs suggests there is strong selective pressure at initiation for tumors to retain NFIB in this mouse model. *RPM* mice die at a median of 60 days after tumor initiation from their tumor burden, and at that time, *RPM;Nfib*$^{f/f}$ mutant lungs had significantly lower tumor burden by area compared to *RPM* mutant lungs (Fig. 3E,F). As a result, *RPM;Nfib*$^{f/f}$ mutant mice survived longer before succumbing to their lung tumor burden (Fig. 3G,H). At the time of death, some large tumors in *RPM;Nfib*$^{f/f}$ mutant lungs were NFIB^{neg} (Fig. 3I) and had similarly near-ubiquitous Ki67 positive staining as NFIB^{high} tumors (Fig. 3J), possibly using an alternate molecular mechanism to increase proliferation in place of NFIB. Human cell lines with low MYC expression have almost invariably mid-to-high NFIB expression, while cell lines with high MYC expression have a much higher range (Fig. S3) (27), suggesting that the oncogenic expression of MYC allows SCLC cells to grow without a need for NFIB.

These data in *RPM* mutant mice indicate that, similar to the *RPR2* model, the presence of NFIB affects SCLC tumor growth at the time when NFIB levels are elevated, with a more critical role for NFIB at the time of initiation in the *RPM* model. Previous studies in human SCLC cell lines expressing high levels of MYC also showed that NFIB is required for the growth of these cell lines (20), and its overexpression is sufficient to promote further growth (19). These observations support the role of NFIB as an oncogenic driver of SCLC in different subtypes of this cancer.

The rapid death of *RPM* mutant mice and the frequent retention of NFIB in *RPM;Nfib*$^{f/f}$ mutant mice, however, made it difficult to conclusively determine the role of NFIB in metastatic progression in this model. While mice in the *RPM* model develop metastases with high NFIB expression (18), we rarely found metastases at morbidity in our *RPM* or *RPM;Nfib*$^{f/f}$ mutant mice. Furthermore, because of the presence of NFIB^{high} *RPM;Nfib*$^{f/f}$ primary tumors, we would not have been able to determine if any NFIB^{high} metastases in *RPM;Nfib*$^{f/f}$ mice arose because NFIB was contributing to metastatic ability or by chance from primary tumors that retained NFIB expression. Thus, we decided to pursue our investigation of NFIB in SCLC metastatic progression solely in *RPR2* mutant mice.

NFIB is not required for EMT in the RPR2 mouse model of SCLC-A

E-Cadherin/CDH1 is a marker of epithelial cells and is involved in cell adhesion (48,49). In SCLC and other cancers, CDH1 expression is inversely correlated with an epithelial-to-mesenchymal transition (EMT) signature (48,50), and low CDH1 levels have been associated with poorer survival in patients with SCLC (51). In mouse models of SCLC-A, primary tumors are mostly NFIB^{low} CDH1^{high}, and upregulation of NFIB during tumor progression has been found to correlate with low levels of CDH1 (22,52).

Consistent with those previous results, primary tumors in the lungs of *RPR2* and *RPR2;Nfib*$^{f/f}$ mutant mice were CDH1^{high} at an early time point (Fig. S4A). At morbidity, lung tumors in *RPR2* mutant mice showed the expected heterogeneity in CDH1 expression, with a shift towards NFIB^{high} CDH1$^{low/neg}$ tumors (Fig. S4B), and the majority of liver metastases were CDH1^{neg} (Fig. S2C,D). Notably, in *RPR2;Nfib*$^{f/f}$ mutant lungs, tumors

showed a similar heterogeneity in CDH1 expression despite being entirely NFIB^{neg} (Fig. S4B), and NFIB^{neg} metastases in *RPR2;Nfib$^{f/f}$* mutant livers expressed a range of CDH1 expression levels by immunostaining (Fig. S4C,D). Thus, while NFIB^{neg} metastases in *RPR2;Nfib$^{f/f}$* mutant mice had higher levels of CDH1 on average, the large proportion of CDH1$^{low/neg}$ tumors suggests that SCLC tumors can gain more mesenchymal features independently of NFIB levels. Furthermore, in *RPR2* and *RPR2;Nfib$^{f/f}$* mutant mice, the presence of metastases with high levels of CDH1 indicates that sustained loss of CDH1 is not absolutely required for metastatic progression.

Together, these data indicate that neither upregulation of NFIB nor loss of CDH1 are necessary for metastatic progression in this mouse model of SCLC, which led us to further investigate molecular phenotypes in NFIB wild-type and knockout SCLC metastases.

NFIB^{neg} tumors are molecularly distinct from NFIB^{high} tumors in the RPR2 model

In mouse models of SCLC-A, late-stage tumors and metastases frequently have genomic rearrangements on chromosome 4, including independent focal amplifications of the *Nfib* and *Mycl* loci, which correlates with high expression levels of NFIB and MYCL (20,22,53). Previous work in the *RP* model has shown that targeted deletion of the *Pten* gene on chromosome 19 is sufficient to abrogate the loss of chromosome 19, which is otherwise frequently observed during tumor progression (53). Similarly, targeted loss of *Nfib* would be expected to prevent amplification of its chromosomal locus, unless other genes near *Nfib* are SCLC drivers that benefit from amplification during tumor progression.

We performed low-pass whole genome sequencing (WGS) on 5 cell lines derived from individual *RPR2;Nfib$^{f/f}$* mutant large primary tumors or liver metastases as well as one *RPR2* mutant cell line (N2N1G) derived from a lymph node metastasis (19) (Fig. 4A). As expected, the *RPR2* mutant cell line N2N1G showed amplification at the *Nfib* locus (Fig. 4B), which correlated with high levels of the NFIB protein (Fig. 4C). Of the *RPR2;Nfib$^{f/f}$* mutant cell lines analyzed, 4/5 did not amplify the chromosomal region including the *Nfib* locus (Fig. 4B and Fig. S5A), and 0/5 cell lines had elevated protein levels of NFIB (Fig. 4C), indicating that loss of *Nfib* decreases the selective pressure for amplification of this locus. One of the *RPR2;Nfib$^{f/f}$* mutant cell lines showed amplification of the *Nfia* locus, also on chromosome 4 (Fig. 4B). This observation suggests that this family member of *Nfib* may sometimes compensate for the inability of these cells to upregulate *Nfib*, as suggested before in other contexts (54,55), but we did not pursue the analysis of NFIA function in this cell line. None of the cell lines analyzed showed focal amplification of the other NFI family members (*Nfic* located on chromosome 10*, Nfix* located on chromosome 8) (Fig. 4D).Of the *RPR2;Nfib$^{f/f}$* cell lines, 2/5 showed loss of chromosome 19 where *Pten* is located, and 3/5 showed focal amplification of *Mycl* (Fig. 4D), as previously described in *RP* mutant tumors (53). While the number of samples we analyzed were limited, the observed heterogeneity suggested that the ability to metastasize without NFIB is not limited to tumors driven by a specific known chromosomal alteration.

In *RPR2* mutant tumors, amplification of *Nfib* and upregulation of NFIB have been associated with changes in genes programs related to cell motility, cell migration, and neuronal differentiation, which may all partly contribute to the enhanced metastatic ability

of NFIB^{high} cells (19,33). To determine if similar gene programs were being upregulated during metastasis in *RPR2;Nfib$^{f/f}$* mutant tumors in the absence of NFIB upregulation, we compared gene expression programs in macrodissected *RPR2* and *RPR2;Nfib$^{f/f}$* mutant lung tumors and liver metastases by RNA sequencing (RNA-seq). *RPR2* mutant metastases clustered separately from *RPR2;Nfib$^{f/f}$* mutant metastases, indicating that the tumors were transcriptionally distinct (Fig. 4E and S5B). We compared the genes that were differentially up- or downregulated between primary tumors and metastases in *RPR2* and in *RPR2;Nfib$^{f/f}$* mutant mice and found little overlap (Fig. S5C and Table S2). The genes that did overlap were primarily liver or lung-specific (Fig. S5D and Table S3), likely due to the presence of contaminating normal lung or liver tissue in the tumor samples collected by macrodissection. Genes that were upregulated in metastases compared to primary tumors in *RPR2* mutant mice were enriched for neuronal terms as expected (19,33) (Fig. 4F and Table S3), whereas genes upregulated in *RPR2;Nfib$^{f/f}$* mutant metastases compared to primary tumors were enriched for cell cycle terms (Fig. 4G and Table S3). To specifically interrogate neuronal enrichment between primary and metastatic tumors, we performed Gene Set Enrichment Analysis (GSEA) on the differentially expressed genes using an axon-related gene signature expressed in SCLC (33). We found that unlike in *RPR2* mutant mice, the axon-related signature is not enriched in *RPR2;Nfib$^{f/f}$* mutant metastases compared to *RPR2;Nfib$^{f/f}$* mutant primary tumors (Fig. S5E and Table S4).

These DNA and RNA analyses suggest that the NFIB^{neg} SCLC cells that metastasize have gained some proliferative potential compared to cells in *RPR2;Nfib$^{f/f}$* mutant primary tumors, but they did not readily identify mechanisms underlying this potential or the ability of NFIB^{neg} SCLC cells to metastasize.

NFIB^{neg} metastases display a chromatin signature associated with ASCL1 and FOXA1/2 activity

In *RPR2* mutant tumors, upregulation of NFIB is associated with an increase in global chromatin accessibility at NFIB binding sites; in our previous ATAC-seq (Assay for Transposase-Accessible Chromatin followed by sequencing) analysis, over 20,000 sites were differentially open between NFIB^{high} metastases and NFIB^{low} primary tumors (19). We wondered if the analysis of chromatin accessibility in *RPR2;Nfib$^{f/f}$* mutant tumors and metastases may reveal a similar increase in chromatin accessibility during metastatic progression and/or point to factors implicated in the metastasis of NFIB^{neg} SCLC cells. We performed an ATAC-seq analysis of cell lines from individual lung tumors and liver metastases from *RPR2;Nfib$^{f/f}$* mutant mice, using cell lines from liver and lymph node metastases from *RPR2* mutant mice as controls. This analysis showed few differences between metastases and primary tumors in the *RPR2;Nfib$^{f/f}$* model (Fig. 5A), as well as large differences between metastases when comparing the *RPR2;Nfib$^{f/f}$* model against the *RPR2* model (Fig. 5B). As expected, *RPR2;Nfib$^{f/f}$* mutant metastases showed less accessibility at peaks previously found to be associated with NFIB (19) compared to *RPR2* mutant metastases (Fig. S6A). *RPR2* mutant metastases clustered separately from *RPR2;Nfib$^{f/f}$* metastases, suggesting that their chromatin state is not a shared phenotype of metastasis (Fig. 5C and Fig. S6B). Overall, metastatic progression in the absence of NFIB does not involve the increase in global accessibility characteristic of NFIB upregulation.

To identify candidate transcriptional regulators that might be contributing to metastasis in *RPR2;Nfib*$^{f/f}$ mutant mice, we searched for binding motifs enriched in regions that were more accessible in *RPR2;Nfib*$^{f/f}$ mutant metastases compared to *RPR2;Nfib*$^{f/f}$ mutant primary tumors (Fig. 5D and Table S5) or *RPR2* mutant metastases (Fig. 5E and Table S5). The comparison between *RPR2;Nfib*$^{f/f}$ mutant metastases and *RPR2;Nfib*$^{f/f}$ mutant primary tumors (Fig. 5D and Table S5) identified an enrichment for binding sites for basic helix-loop-helix (bHLH) transcription factors (group A, (56)). Our RNA-seq analysis shows that of the bHLH factors with enriched motifs, only ASCL1, TCF3, TCF4, and TCF12 are expressed in our SCLC-A tumors (Fig. S6B and Table S5). ASCL1 is the only one expressed at high levels, and TCF3, TCF4, and TCF12 are known heterodimer partners for ASCL1 (57,58). ASCL1 is a known driver of SCLC development (59,60), so our enrichment analysis suggests that *RPR2;Nfib*$^{f/f}$ mutant tumors rely on ASCL1 activity to progress and metastasize. The comparison between *RPR2;Nfib*$^{f/f}$ mutant metastases and *RPR2* mutant metastases (Fig. 5E and Table S5) identified an enrichment for motifs for the FOX and SOX families of transcription factors. Of the top enriched motifs, the transcription factors expressed in SCLC-A tumors in our RNA-seq analysis are FOXA1, FOXA2, FOXM1, and SOX2 (Fig. S6C and Table S5). FOXM1 and SOX2 are both ASCL1 targets (59,61) and have oncogenic roles in SCLC (62,63). Similarly, FOXA1 and FOXA2 have both been shown to be part of the ASCL1 regulatory network in SCLC-A tumors (57,60), which further supports the importance of the ASCL1 network in *RPR2;Nfib*$^{f/f}$ mutant tumors.

To further investigate possible changes in the activity of FOXA1/2 factors in SCLC metastases with no NFIB, we performed a Cleavage Under Targets and Release Using Nuclease (CUT&RUN) (64) analysis for FOXA1 in two of the cell lines on which we performed the ATAC-seq analysis: N2N1G (cell line from an *RPR2* mutant metastasis) and 1399M2 (cell line from an *RPR2;Nfib*$^{f/f}$ mutant metastasis). First, we identified a consensus peak set from the open chromatin regions in the ATAC-seq analyses (Fig. 5C, S7A). FOXA1 binding to this consensus peak set was marginally higher overall in 1399M2 compared to N2N1G (Fig. 6A,B). When we focused on chromatin regions that were differentially accessible between N2N1G and 1399M2, we found that at sites differentially open in N2N1G, FOXA1 binding was enriched in N2N1G compared to 1399M2 (Fig. 6C and Fig. S7B), and at sites differentially open in 1399M2, FOXA1 binding was enriched in 1399M2 compared to N2N1G (Fig. 6D and Fig. S7C). In tandem, these suggest that FOXA1 binding is independently involved in chromatin accessibility in both N2N1G and 1399M2. Furthermore, when we analyzed consensus binding motifs for transcription factors at FOXA1 binding sites, we found FOXA binding motifs as expected in both N2N1G and 1399M2 (Fig. 6E,F and Table S6). In contrast, NFI binding motifs were enriched at FOXA1 binding site in N2N1G (Fig. 6E and Table S6), but not in 1399M2 (Fig. 6F and Table S6).

Thus, SCLC-A cells can metastasize by turning on an “NFIB switch”, potentially in conjunction with FOXA1/2. When this switch is not possible, these cells rely on oncogenic programs centered around the ASCL1 and the FOXA1/2 transcription factors (Fig. 6G).

Discussion

Metastases are a major cause of morbidity and mortality in patients with SCLC. Clinical progress for this recalcitrant cancer is thus likely to come from a better understanding of the mechanisms that allow SCLC cells to metastasize. The identification of NFIB as a pro-metastatic oncogene in a majority of SCLC cases (19,22) has provided for the first time a molecular handle to comprehend metastatic progression in this fatal disease. Here we sought to determine if NFIB is required for SCLC cells to gain metastatic potential. To this end, we used relevant mouse models in which upregulation of NFIB is associated with tumor growth and metastasis. Our results conclusively show that there is no absolute requirement for NFIB in these models for metastasis. These observations underscore the highly plastic nature of SCLC and the ability of SCLC cells to take various molecular paths during tumor progression.

NFIB is not required for the growth of NFIB^{high} SCLC populations in culture or in subcutaneous tumors, but SCLC cells in circulation rely on NFIB to successfully metastasize to the liver (19). One mechanism underlying this requirement for liver metastasis may originate from some of the neuronal features of NFIB^{high} cells, which have been linked to new migratory capabilities (33). NFIB is also required for optimal growth of SCLC cells in the brain microenvironment, which again can be linked to neuronal features of NFIB^{high} SCLC cells (65). Our new data with the same *RPR2* model indicate that NFIB plays a role in the growth of primary tumors in the lungs, especially after NFIB levels are upregulated during tumor progression, and the decreased growth of NFIB^{neg} tumors in this context is correlated with a decreased proliferative potential. It is thus possible that some of the pro-metastatic effects of NFIB simply come from its pro-proliferative role, which becomes more visible in comparison to NFIB^{neg} tumors. A similar role for NFIB in proliferation has been observed before in mouse and human SCLC cells in culture (20,23), including MYC-driven human SCLC cell lines with varying levels of NFIB (19,20). In the MYC-driven *RPM* mouse model, the high Ki67 expression we found in late NFIB^{neg} tumors suggests that MYC-driven SCLC may be less reliant on NFIB to increase proliferation, but NFIB may still play a critical role in tumor progression, as we also observed a strong pressure to retain NFIB expression at the time of initiation.

Recent work has further shown that methylation of NFIB by the CARM1 methyltransferase promotes the oncogenic potential of NFIB in the *RPR2* model; a germline knock-in mutation in this methylation site inhibits tumor progression and metastasis (21). Notably, the inhibition of metastasis in this model was observed at an earlier time point when there was a still a difference in primary tumor burden. In contrast, all of our metastatic tumors were collected at morbidity While we did not measure metastatic burden at a set time point, it is likely that we would have seen a similar difference in metastatic tumor burden between *RPR2* and *RPR2;Nfib*$^{f/f}$ mutant mice.

Altogether, these data indicate that NFIB has oncogenic and pro-metastatic roles in multiple contexts, including *via* its role as a pro-proliferative factor and as a pro-neuronal factor. These data also support the notion that NFIB may remain a viable therapeutic target in

SCLC. The development of strategies such as small molecule degraders (66) offers new possibilities to target this transcription factor in developing tumors and in metastases.

Our ATAC-seq data have identified ASCL1 and FOXA1/2 as candidate regulators of the metastatic process in SCLC cells in which NFIB levels cannot be upregulated. ASCL1 expression is not only the defining characteristic of SCLC-A tumors, but also necessary for the development of neuroendocrine SCLC (59,60). ASCL1 can directly activate cell cycle factors such as E2F and FOXM1 (61,67) and known SCLC oncogenes such as SOX2 and MYCL (57,59). It is likely that enhanced ASCL1 activity can promote tumor progression through multiple mechanisms in its transcriptional network, including FOXA1 and FOXA2. In SCLC, ASCL1, FOXA1, and FOXA2 expression are positively correlated (59,60), and FOXA motifs are enriched at ASCL1 binding sites (59), suggesting these three factors may co-localize to regulate oncogenic transcriptional networks.

FOXA1 has roles in multiple cancers, notably other neuroendocrine cancers (68,69), and works as a pioneer factor in conjunction with many other transcriptional regulators (70). In prostate cancer, FOXA1 and ASCL1 are known to co-localize on regulatory regions to promote the transition from prostate adenocarcinoma to neuroendocrine prostate cancer, and these FOXA1-bound regulatory regions are similarly H3K27-acetylated in SCLC (71). FOXA2 has long been known to be expressed in SCLC (72), and FOXA2 is itself an ASCL1 target (59,60). FOXA2 levels have been found to be high in cell lines derived from SCLC circulating tumor cells (73), and human SCLC cell lines are dependent on FOXA2 for their growth in culture (57). Notably, our previous ATAC-seq analysis had found FOXA1/2 binding motifs enriched at NFIB binding sites in metastases from the *RPR2* model (19), which initially suggested a model in which it may be acting as a pioneer factor to promote NFIB binding. This is further supported by our CUT&RUN analysis, which shows NFI binding motifs enriched in FOXA1 binding sites in a cell line derived from an *RPR2* metastasis. FOXA1/2 can also potentially promote tumor progression in the absence of NFIB, as our CUT&RUN data suggest that FOXA1 is bound at independent chromatin regions that are differentially accessible in both *RPR2* and *RPR2;Nfib*$^{f/f}$ tumors. Thus, FOXA1/2 may be critical in SCLC metastasis in both NFIB-dependent and NFIB-independent contexts. It will be important in future studies to investigate the consequences of manipulating FOXA1 and FOXA2 during tumor progression and metastasis in relevant models, including models for not only SCLC-A but also other SCLC subtypes with low or no ASCL1 expression, similar to what has been done previously in lung adenocarcinoma (74).

The vast majority of metastatic tumors in the Ad-CMV-Cre *RPR2* model upregulate NFIB (19). In these tumors, FOXA1/2 may facilitate NFIB binding at new sites throughout the genome to increase chromatin accessibility, proliferation, and pro-metastatic and neuronal gene programs (Fig. 5**G**, top). NFIB upregulation accelerates tumor progression and metastasis, and the resulting decrease in survival limits the window of opportunity for tumors that do not upregulate NFIB to metastasize. If given enough time, cells that do not or cannot upregulate NFIB may progress through an NFIB-independent model of metastasis by relying on their high ASCL1, FOXA1, or FOXA2 expression. The ASCL1 transcriptional network includes multiple oncogenic mechanisms, including cell cycle regulation, and

FOXA1/2 binding may also play an important and possibly independent role in regulating chromatin accessibility(Fig. 5G, bottom).

Metastatic tumors with NFIB deletion may have been expected to follow an evolutionary path that is dominated by one alternative mechanism. For example, upregulation of a family member of NFIB such as NFIA could have been a recurrent mechanism, especially since *Nfia* is on the same chromosomal region as *Nfib*. However, our low-pass whole genome sequencing, RNA sequencing, and chromatin analyses do not support the existence of a single major alternative mechanism (for example, just one of five tumors amplified *Nfia*, and we did not investigate other NFI family members). Furthermore, amplification of *Nfia* does not appear to be directly compensatory for amplification of *Nfib*, as the cell line with the *Nfia* amplification (1399M2) did not show enrichment of the NFI family consensus motifs at FOXA1 binding sites (Fig. 6F). Instead, our data suggest that NFIB mutant tumors can take various paths during tumor progression and metastasis. These paths may be different from metastases in the same *RPR2* model where tumors are initiated by Ad-CGRP-Cre, targeting specifically pulmonary neuroendocrine cells. In this model, NFIB is less frequently upregulated during tumor progression, but metastases also upregulate neuronal programs compared to primary tumors (unlike $NFIB^{neg}$ tumors, in which the only signature observed is a cell cycle signature) (24). This ability to reach a diversity of genetic and transcriptional states during tumor progression and metastasis is reminiscent of the mechanisms of resistance to treatment (e.g., chemotherapy), where resistant cancer cells reach transcriptional states that are more diverse than naïve tumors (75). These observations underscore the need for better analysis of SCLC heterogeneity both during tumor progression and in response to treatment.

Acknowledgments

We thank Alyssa Ray for administrative support; Dr. Trudy Oliver for sharing the *RPM* mouse model; Dr. Richard Gronostajski for sharing the $Nfib^{flox}$ mouse model; Pauline Chu and the Animal Histology Service Center at Stanford University for help with histology; the Stanford Shared FACS Facility for flow cytometry services (NIH S10 Shared Instrument Grant S10RR027431-01); the Stanford Veterinary Service Center for expert animal care; the Stanford Genomics Service Center as well as the Protein and Nucleic Acid Facility for help with Bioanalyzer runs; members of the laboratory of J.S. for their help and support throughout this study. This work was supported by the NIH (J.S., CA231997 and J.H.K., F31CA257169-01, and P30-CA124435 to the Stanford Cancer institute). M.C.L. was supported by a Tom and Susan Ford Stanford Graduate Fellowship in Science and Engineering and a Tobacco-Related Disease Research Program (TRDRP) Predoctoral Fellowship (T32DT4747). D.B. is a fellow of the Damon Runyon Cancer Research Foundation (DRG-2466-22). J.S. is the Elaine and John Chambers Professor in Pediatric Cancer.

Supplementary Material

Refer to Web version on PubMed Central for supplementary material.

Financial support:

This work was supported by the NIH (J.S., CA231997 and J.H.K., CA257169, and CA124435 to the Stanford Cancer institute). M.C.L. was supported by a Tom and Susan Ford Stanford Graduate Fellowship in Science and Engineering and a Tobacco-Related Disease Research Program (TRDRP) Predoctoral Fellowship (T32DT4747). D.B. is a fellow of the Damon Runyon Cancer Research Foundation (DRG-2466-22).

References

1. Fares J, Fares MY, Khachfe HH, Salhab HA, Fares Y. Molecular principles of metastasis: a hallmark of cancer revisited. Signal Transduct Target Ther. 2020;5:28. [PubMed: 32296047]
2. Ganesh K, Massagué J. Targeting metastatic cancer. Nat Med. 2021;27:34–44. [PubMed: 33442008]
3. Lambert AW, Pattabiraman DR, Weinberg RA. Emerging Biological Principles of Metastasis. Cell. Cell Press; 2017;168:670–91. [PubMed: 28187288]
4. Nguyen DX, Bos PD, Massagué J. Metastasis: From dissemination to organ-specific colonization. Nature Reviews Cancer. Nature Publishing Group; 2009;9:274–84. [PubMed: 19308067]
5. Rudin CM, Brambilla E, Faivre-Finn C, Sage J. Small-cell lung cancer. Nature Reviews Disease Primers. 2021;7:1–20.
6. Ko J, Winslow MM, Sage J. Mechanisms of small cell lung cancer metastasis. EMBO Mol Med. 2021;13:e13122. [PubMed: 33296145]
7. Byers LA, Rudin CM. Small cell lung cancer: Where do we go from here? Cancer. John Wiley and Sons Inc.; 2015;121:664–72. [PubMed: 25336398]
8. Gazdar AF, Bunn PA, Minna JD. Small-cell lung cancer: what we know, what we need to know and the path forward. Nature Reviews Cancer. 2017;17:725–37. [PubMed: 29077690]
9. Farago AF, Yeap BY, Stanzione M, Hung YP, Heist RS, Marcoux JP, et al. Combination Olaparib and Temozolomide in Relapsed Small-Cell Lung Cancer. Cancer Discov. 2019;9:1372–87. [PubMed: 31416802]
10. Hodgkinson CL, Morrow CJ, Li Y, Metcalf RL, Rothwell DG, Trapani F, et al. Tumorigenicity and genetic profiling of circulating tumor cells in small-cell lung cancer. Nature Medicine. Nature Publishing Group; 2014;20:897–903.
11. George J, Lim JS, Jang SJ, Cun Y, Ozretia L, Kong G, et al. Comprehensive genomic profiles of small cell lung cancer. Nature. Nature Publishing Group; 2015;524:47–53. [PubMed: 26168399]
12. Ferone G, Lee MC, Sage J, Berns A. Cells of origin of lung cancers: Lessons from mouse studies. Genes and Development. Genes Dev; 2020;34:1017–32. [PubMed: 32747478]
13. Meuwissen R, Linn SC, Linnoila RI, Zevenhoven J, Mooi WJ, Berns A. Induction of small cell lung cancer by somatic inactivation of both Trp53 and Rb1 in a conditional mouse model. Cancer Cell. Cell Press; 2003;4:181–9. [PubMed: 14522252]
14. Gazdar AF, Savage TK, Johnson JE, Berns A, Sage J, Linnoila RI, et al. The comparative pathology of genetically engineered mouse models for neuroendocrine carcinomas of the lung. Journal of Thoracic Oncology. Lippincott Williams and Wilkins; 2015;10:553–64. [PubMed: 25675280]
15. Schaffer BE, Park KS, Yiu G, Conklin JF, Lin C, Burkhart DL, et al. Loss of p130 accelerates tumor development in a mouse model for human small-cell lung carcinoma. Cancer Research. 2010;70:3877–83. [PubMed: 20406986]
16. Rudin CM, Poirier JT, Byers LA, Dive C, Dowlati A, George J, et al. Molecular subtypes of small cell lung cancer: a synthesis of human and mouse model data. Nat Rev Cancer. 2019;19:289–97. [PubMed: 30926931]
17. Dammert MA, Brägelmann J, Olsen RR, Böhm S, Monhasery N, Whitney CP, et al. MYC paralog-dependent apoptotic priming orchestrates a spectrum of vulnerabilities in small cell lung cancer. Nature Communications. 2019;10.
18. Mollaoglu G, Guthrie MR, Böhm S, Brägelmann J, Can I, Ballieu PM, et al. MYC Drives Progression of Small Cell Lung Cancer to a Variant Neuroendocrine Subtype with Vulnerability to Aurora Kinase Inhibition. Cancer Cell. 2017;31:270–85. [PubMed: 28089889]

19. Denny SK, Yang D, Chuang C-H, Brady JJ, Lim JS, Grüner BM, et al. Nfib Promotes Metastasis through a Widespread Increase in Chromatin Accessibility. Cell. Elsevier; 2016;166:328–42. [PubMed: 27374332]
20. Dooley AL, Winslow MM, Chiang DY, Banerji S, Stransky N, Dayton TL, et al. Nuclear factor I/B is an oncogene in small cell lung cancer. Genes & Development. 2011;25:1470–5. [PubMed: 21764851]
21. Gao G, Hausmann S, Flores NM, Benitez AM, Shen J, Yang X, et al. The NFIB/CARM1 partnership is a driver in preclinical models of small cell lung cancer. Nat Commun. 2023;14:363. [PubMed: 36690626]
22. Semenova EA, Kwon M chul, Monkhorst K, Song JY, Bhaskaran R, Krijgsman O, et al. Transcription Factor NFIB Is a Driver of Small Cell Lung Cancer Progression in Mice and Marks Metastatic Disease in Patients. Cell Reports. Elsevier; 2016;16:631–43. [PubMed: 27373156]
23. Wu N, Jia D, Ibrahim AH, Bachurski CJ, Gronostajski RM, Macpherson D. NFIB overexpression cooperates with Rb/p53 deletion to promote small cell lung cancer. Oncotarget. Impact Journals, LLC; 2016;7:57514–24. [PubMed: 27613844]
24. Yang D, Denny SK, Greenside PG, Chaikovsky AC, Brady JJ, Ouadah Y, et al. Intertumoral heterogeneity in SCLC is influenced by the cell type of origin. Cancer Discovery. American Association for Cancer Research Inc.; 2018;8:1316–31. [PubMed: 30228179]
25. Steele-Perkins G, Plachez C, Butz KG, Yang G, Bachurski CJ, Kinsman SL, et al. The Transcription Factor Gene Nfib Is Essential for both Lung Maturation and Brain Development. Molecular and Cellular Biology. 2005;25:685–98. [PubMed: 15632069]
26. Ruifrok AC, Johnston DA. Quantification of histochemical staining by color deconvolution. Anal Quant Cytol Histol. 2001;23:291–9. [PubMed: 11531144]
27. Tlemsani C, Pongor L, Elloumi F, Girard L, Huffman KE, Roper N, et al. SCLC-CellMiner: A Resource for Small Cell Lung Cancer Cell Line Genomics and Pharmacology Based on Genomic Signatures. Cell Rep. 2020;33:108296. [PubMed: 33086069]
28. Patro R, Duggal G, Love MI, Irizarry RA, Kingsford C. Salmon provides fast and bias-aware quantification of transcript expression. Nat Methods. 2017;14:417–9. [PubMed: 28263959]
29. Love MI, Huber W, Anders S. Moderated estimation of fold change and dispersion for RNA-seq data with DESeq2. Genome Biol. 2014;15:550. [PubMed: 25516281]
30. Mootha VK, Lindgren CM, Eriksson K-F, Subramanian A, Sihag S, Lehar J, et al. PGC-1α-responsive genes involved in oxidative phosphorylation are coordinately downregulated in human diabetes. Nat Genet. Nature Publishing Group; 2003;34:267–73. [PubMed: 12808457]
31. Subramanian A, Tamayo P, Mootha VK, Mukherjee S, Ebert BL, Gillette MA, et al. Gene set enrichment analysis: A knowledge-based approach for interpreting genome-wide expression profiles. Proceedings of the National Academy of Sciences. Proceedings of the National Academy of Sciences; 2005;102:15545–50.
32. Reich M, Liefeld T, Gould J, Lerner J, Tamayo P, Mesirov JP. GenePattern 2.0. Nat Genet. 2006;38:500–1. [PubMed: 16642009]
33. Yang D, Qu F, Cai H, Chuang CH, Lim JS, Jahchan N, et al. Axon-like protrusions promote small cell lung cancer migration and metastasis. eLife. eLife Sciences Publications Ltd; 2019;8.
34. Chen EY, Tan CM, Kou Y, Duan Q, Wang Z, Meirelles GV, et al. Enrichr: interactive and collaborative HTML5 gene list enrichment analysis tool. BMC Bioinformatics. 2013;14:128. [PubMed: 23586463]
35. Kuleshov MV, Jones MR, Rouillard AD, Fernandez NF, Duan Q, Wang Z, et al. Enrichr: a comprehensive gene set enrichment analysis web server 2016 update. Nucleic Acids Res. 2016;44:W90–97. [PubMed: 27141961]
36. Xie Z, Bailey A, Kuleshov MV, Clarke DJB, Evangelista JE, Jenkins SL, et al. Gene Set Knowledge Discovery with Enrichr. Curr Protoc. 2021;1:e90. [PubMed: 33780170]
37. Bolger AM, Lohse M, Usadel B. Trimmomatic: a flexible trimmer for Illumina sequence data. Bioinformatics. 2014;30:2114–20. [PubMed: 24695404]
38. Li H, Durbin R. Fast and accurate long-read alignment with Burrows-Wheeler transform. Bioinformatics. 2010;26:589–95. [PubMed: 20080505]

39. Talevich E, Shain AH, Botton T, Bastian BC. CNVkit: Genome-Wide Copy Number Detection and Visualization from Targeted DNA Sequencing. PLoS Comput Biol. 2016;12:e1004873. [PubMed: 27100738]
40. Corces MR, Trevino AE, Hamilton EG, Greenside PG, Sinnott-Armstrong NA, Vesuna S, et al. An improved ATAC-seq protocol reduces background and enables interrogation of frozen tissues. Nat Methods. 2017;14:959–62. [PubMed: 28846090]
41. Langmead B, Salzberg SL. Fast gapped-read alignment with Bowtie 2. Nat Methods. 2012;9:357–9. [PubMed: 22388286]
42. Li H, Handsaker B, Wysoker A, Fennell T, Ruan J, Homer N, et al. The Sequence Alignment/Map format and SAMtools. Bioinformatics. 2009;25:2078–9. [PubMed: 19505943]
43. Zhang Y, Liu T, Meyer CA, Eeckhoute J, Johnson DS, Bernstein BE, et al. Model-based Analysis of ChIP-Seq (MACS). Genome Biol. 2008;9:R137. [PubMed: 18798982]
44. Stark Rory, Brown Gord. DiffBind: differential binding analysis of ChIP-Seq peak data [Internet]. 2011 [cited 2023 Mar 16]. Available from: http://bioconductor.org/packages/release/bioc/vignettes/DiffBind/inst/doc/DiffBind.pdf
45. Ramírez F, Ryan DP, Grüning B, Bhardwaj V, Kilpert F, Richter AS, et al. deepTools2: a next generation web server for deep-sequencing data analysis. Nucleic Acids Res. 2016;44:W160–165. [PubMed: 27079975]
46. Lim JS, Ibaseta A, Fischer MM, Cancilla B, O'Young G, Cristea S, et al. Intratumoural heterogeneity generated by Notch signalling promotes small-cell lung cancer. Nature. 2017;545:360–4. [PubMed: 28489825]
47. Shue YT, Drainas AP, Li NY, Pearsall SM, Morgan D, Sinnott-Armstrong N, et al. A conserved YAP/Notch/REST network controls the neuroendocrine cell fate in the lungs. Nat Commun. Nature Publishing Group; 2022;13:1–18. [PubMed: 34983933]
48. Dongre A, Weinberg RA. New insights into the mechanisms of epithelial–mesenchymal transition and implications for cancer. Nat Rev Mol Cell Biol. Nature Publishing Group; 2019;20:69–84. [PubMed: 30459476]
49. Guillot C, Lecuit T. Mechanics of Epithelial Tissue Homeostasis and Morphogenesis. Science. American Association for the Advancement of Science; 2013;340:1185–9. [PubMed: 23744939]
50. Stewart CA, Tong P, Cardnell RJ, Sen T, Li L, Gay CM, et al. Dynamic variations in epithelial-to-mesenchymal transition (EMT), ATM, and SLFN11 govern response to PARP inhibitors and cisplatin in small cell lung cancer. Oncotarget. Impact Journals LLC; 2017;8:28575–87. [PubMed: 28212573]
51. Chang MH, Lee K, Lee KY, Kim YS, Kim YK, Kang JH. Prognostic role of integrin β 1, E-cadherin, and rac1 expression in small cell lung cancer. APMIS. APMIS; 2012;120:28–38. [PubMed: 22151306]
52. Böttger F, Semenova EA, Song JY, Ferone G, van der Vliet J, Cozijnsen M, et al. Tumor Heterogeneity Underlies Differential Cisplatin Sensitivity in Mouse Models of Small-Cell Lung Cancer. Cell Reports. Cell Press; 2019;27:3345–3358.e4. [PubMed: 31189116]
53. McFadden DG, Papagiannakopoulos T, Taylor-Weiner A, Stewart C, Carter SL, Cibulskis K, et al. Genetic and clonal dissection of murine small cell lung carcinoma progression by genome sequencing. Cell. 2014;156:1298–311. [PubMed: 24630729]
54. Bunt J, Osinski JM, Lim JW, Vidovic D, Ye Y, Zalucki O, et al. Combined allelic dosage of Nfia and Nfib regulates cortical development. Brain Neurosci Adv. 2017;1:2398212817739433. [PubMed: 32166136]
55. Mason S, Piper M, Gronostajski RM, Richards LJ. Nuclear factor one transcription factors in CNS development. Molecular Neurobiology. Humana Press Inc; 2009;39:10–23. [PubMed: 19058033]
56. Ledent V, Vervoort M. The Basic Helix-Loop-Helix Protein Family: Comparative Genomics and Phylogenetic Analysis. Genome Res. 2001;11:754–70. [PubMed: 11337472]
57. Pozo K, Kollipara RK, Kelenis DP, Rodarte KE, Ullrich MS, Zhang X, et al. ASCL1, NKX2-1, and PROX1 co-regulate subtype-specific genes in small-cell lung cancer. iScience. 2021;24:102953. [PubMed: 34466783]

58. Wedel M, Fröb F, Elsesser O, Wittmann M-T, Lie DC, Reis A, et al. Transcription factor Tcf4 is the preferred heterodimerization partner for Olig2 in oligodendrocytes and required for differentiation. Nucleic Acids Res. 2020;48:4839–57. [PubMed: 32266943]
59. Borromeo MD, Savage TK, Kollipara RK, He M, Augustyn A, Osborne JK, et al. ASCL1 and NEUROD1 Reveal Heterogeneity in Pulmonary Neuroendocrine Tumors and Regulate Distinct Genetic Programs. Cell Reports. 2016;16:1259–72. [PubMed: 27452466]
60. Olsen RR, Ireland AS, Kastner DW, Groves SM, Spainhower KB, Pozo K, et al. ASCL1 represses a SOX9+ neural crest stem-like state in small cell lung cancer. Genes Dev. 2021;35:847–69. [PubMed: 34016693]
61. Castro DS, Martynoga B, Parras C, Ramesh V, Pacary E, Johnston C, et al. A novel function of the proneural factor Ascl1 in progenitor proliferation identified by genome-wide characterization of its targets. Genes Dev. 2011;25:930–45. [PubMed: 21536733]
62. Liang S-K, Hsu C-C, Song H-L, Huang Y-C, Kuo C-W, Yao X, et al. FOXM1 is required for small cell lung cancer tumorigenesis and associated with poor clinical prognosis. Oncogene. Nature Publishing Group; 2021;40:4847–58. [PubMed: 34155349]
63. Rudin CM, Durinck S, Stawiski EW, Poirier JT, Modrusan Z, Shames DS, et al. Comprehensive genomic analysis identifies SOX2 as a frequently amplified gene in small-cell lung cancer. Nat Genet. Nature Publishing Group; 2012;44:1111–6. [PubMed: 22941189]
64. Skene PJ, Henikoff S. An efficient targeted nuclease strategy for high-resolution mapping of DNA binding sites. Elife. 2017;6:e21856. [PubMed: 28079019]
65. Qu F, Cao S, Michno W, Madubata CJ, Puno A, Drainas AP, et al. Neuronal mimicry generates an ecosystem critical for brain metastatic growth of SCLC [Internet]. bioRxiv; 2021 [cited 2023 Mar 13]. page 2021.08.10.455426. Available from: https://www.biorxiv.org/content/10.1101/2021.08.10.455426v1
66. Henley MJ, Koehler AN. Advances in targeting “undruggable” transcription factors with small molecules. Nat Rev Drug Discov. 2021;20:669–88. [PubMed: 34006959]
67. Tsuboyama N, Wang R, Szczepanski AP, Chen H, Zhao Z, Shi L, et al. Therapeutic targeting of BAP1/ASXL3 sub-complex in ASCL1-dependent small cell lung cancer. Oncogene. 2022;41:2152–62. [PubMed: 35194152]
68. Adams EJ, Karthaus WR, Hoover E, Liu D, Gruet A, Zhang Z, et al. FOXA1 mutations alter pioneering activity, differentiation and prostate cancer phenotypes. Nature. Nature Publishing Group; 2019;571:408–12. [PubMed: 31243370]
69. Lavigne M, Menet E, Tille J-C, Lae M, Fuhrmann L, Bonneau C, et al. Comprehensive clinical and molecular analyses of neuroendocrine carcinomas of the breast. Mod Pathol. 2018;31:68–82. [PubMed: 28884749]
70. Palozola KC, Lerner J, Zaret KS. A changing paradigm of transcriptional memory propagation through mitosis. Nat Rev Mol Cell Biol. 2019;20:55–64. [PubMed: 30420736]
71. Baca SC, Takeda DY, Seo J-H, Hwang J, Ku SY, Arafeh R, et al. Reprogramming of the FOXA1 cistrome in treatment-emergent neuroendocrine prostate cancer. Nat Commun. Nature Publishing Group; 2021;12:1979. [PubMed: 33785741]
72. Khoor A, Stahlman MT, Johnson JM, Olson SJ, Whitsett JA. Forkhead box A2 transcription factor is expressed in all types of neuroendocrine lung tumors. Human Pathology. 2004;35:560–4. [PubMed: 15138929]
73. Hamilton G, Hochmair M, Rath B, Klameth L, Zeillinger R. Small cell lung cancer: Circulating tumor cells of extended stage patients express a mesenchymal-epithelial transition phenotype. Cell Adhesion and Migration. Taylor and Francis Inc.; 2016;10:360–7. [PubMed: 26919626]
74. Orstad G, Fort G, Parnell TJ, Jones A, Stubben C, Lohman B, et al. FoxA1 and FoxA2 control growth and cellular identity in NKX2-1-positive lung adenocarcinoma. Developmental Cell. 2022;57:1866–1882.e10. [PubMed: 35835117]
75. Stewart CA, Gay CM, Xi Y, Sivajothi S, Sivakamasundari V, Fujimoto J, et al. Single-cell analyses reveal increased intratumoral heterogeneity after the onset of therapy resistance in small-cell lung cancer. Nat Cancer. 2020;1:423–36. [PubMed: 33521652]

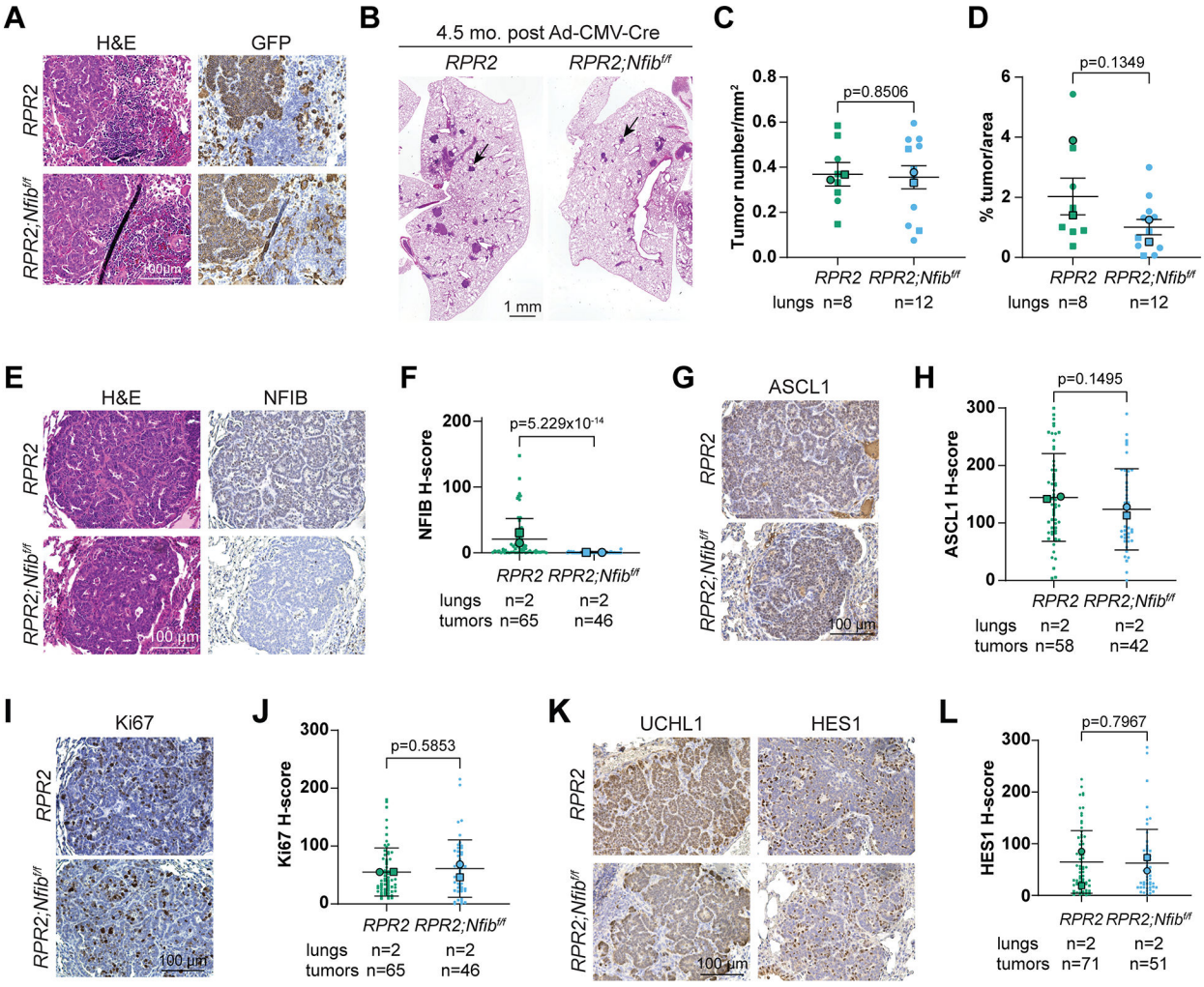

Fig. 1. NFIB is not required for the development of SCLC tumors in the *RPR2* mouse model

A. Representative images of serial sections from *RPR2* and *RPR2;Nfib*$^{f/f}$ mutant tumors stained with H&E (hematoxylin and eosin) or immunostained for GFP (brown signal, with blue hematoxylin counterstain), 4.5 months post Ad-CMV-infection. Scale bar, 100 μm. **B.** Representative images of the lungs of *RPR2* and *RPR2;Nfib*$^{f/f}$ mutant mice stained with H&E, 4.5 months post Ad-CMV-Cre infection. Arrows point to representative tumors. Scale bar, 1mm. **C.** Quantification of (B) for tumor number per mm^2. Here and in (D), tumors were confirmed by GFP immunostaining of serial sections as in (A). Point shapes represent lungs from n=2 cohorts of mice given virus at separate times. Outlined points represent the averages from each cohort. **D.** Quantification of (B) for tumor burden (% tumor area relative to lung area). **E.** Representative images of serial sections from *RPR2* and *RPR2;Nfib*$^{f/f}$ mutant tumors stained with H&E or immunostained for NFIB. Scale bar, 100 μm. **F.** Quantification of NFIB expression from (E). Here and below, point shapes represent tumors from two lung sections, and outlined points represent the averages from each lung. **G.** Representative images of *RPR2* and *RPR2;Nfib*$^{f/f}$ mutant tumors immunostained for ASCL1. Scale bar, 100μm. **H.** Quantification of ASCL1 expression from (G). **I.** Representative images of *RPR2* and *RPR2;Nfib*$^{f/f}$ mutant tumors immunostained for Ki67.

Scale bar, 100 μm. **J.** Quantification of Ki67 expression from (I). **K.** Representative images of *RPR2* and *RPR2;Nfib*$^{f/f}$ mutant tumors immunostained for the neuroendocrine marker UCHL1 or the non-neuroendocrine marker HES1. Scale bar, 100 μm. **L.** Quantification of HES1 expression from (K). All p values calculated by two-tailed Mann-Whitney test. Error bars in (C) and (D) indicate mean ± SEM. Error bars in (F), (H), (J), and (L) indicate mean ± SD.

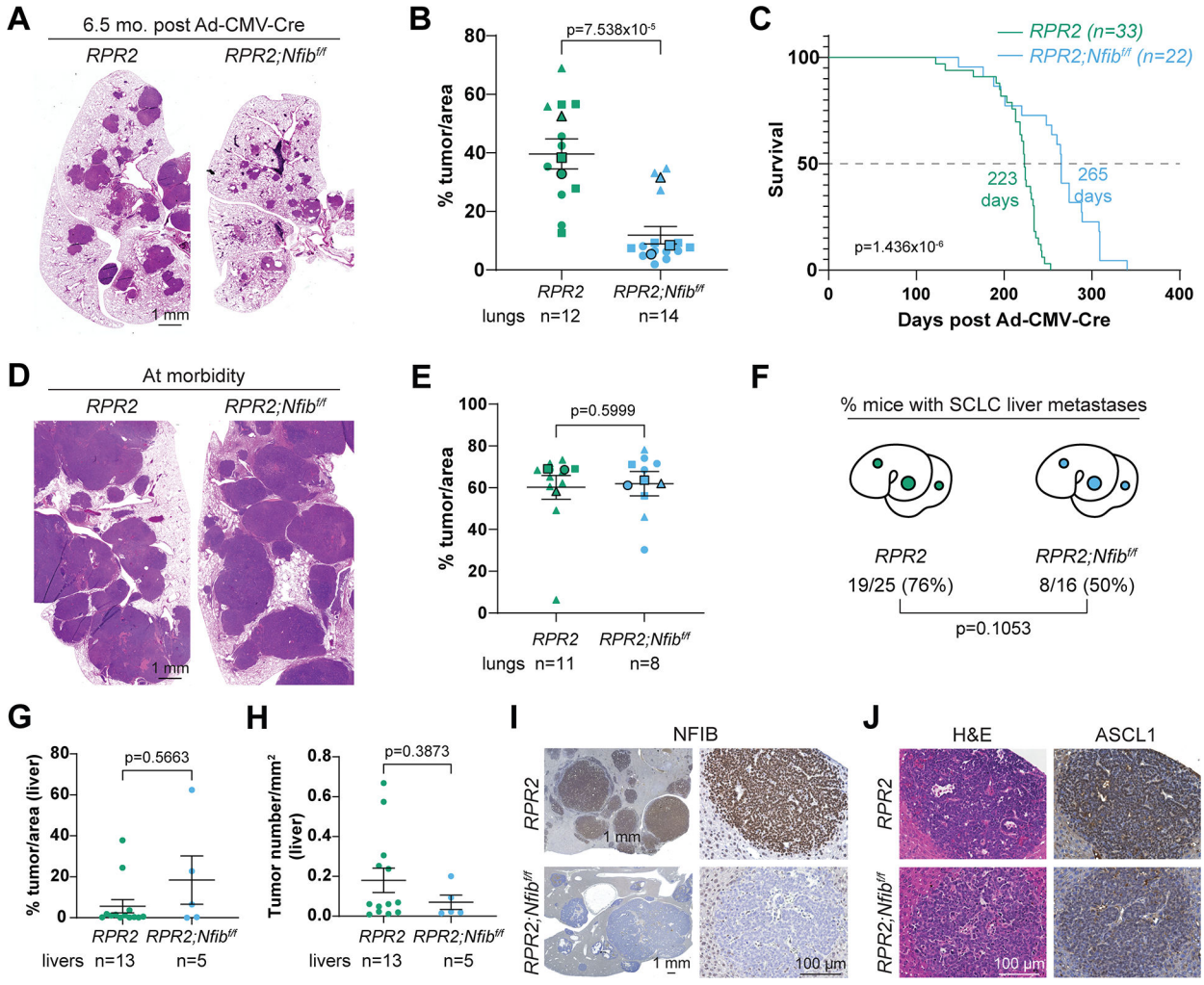

Fig. 2. NFIB contributes to tumor development when upregulated but is not required for metastasis in the *RPR2* mouse model

A. Representative images of *RPR2* and *RPR2;Nfib$^{f/f}$* mutant lungs stained with H&E, 6.5 months post Ad-CMV-Cre infection. Scale bar, 1 mm. **B.** Quantification of (A) for tumor burden. Here and below, point shapes represent lungs from n=3 cohorts of mice given virus at separate times. Outlined points represent the averages from each cohort. **C.** Survival curves and median survival time of *RPR2* and *RPR2;Nfib$^{f/f}$* mutant mice. **D.** Representative images of *RPR2* and *RPR2;Nfib$^{f/f}$* mutant lungs stained with H&E at morbidity. Scale bar, 1 mm. **E.** Quantification of (D) for tumor burden. **F.** Proportion of *RPR2* and *RPR2;Nfib$^{f/f}$* mutant livers with SCLC tumors at morbidity. **G.** Quantification of metastatic tumor burden in *RPR2* and *RPR2;Nfib$^{f/f}$* mutant livers at morbidity. **H.** Quantification of metastatic tumor number per mm^2 in *RPR2* and *RPR2;Nfib$^{f/f}$* mutant livers at morbidity. **I.** Representative images of livers (left) and metastatic tumors (right) from *RPR2* and *RPR2;Nfib$^{f/f}$* mutant mice at morbidity, immunostained for NFIB. Scale bar, 1 mm (left), 100 µm (right). **J.** Representative images of serial sections of metastatic tumors as in (I), stained with H&E or immunostained for ASCL1. Scale bar, 100 µm. P values for (B), (E), (G), and (H) calculated

by two-tailed Mann-Whitney test. P value for (C) calculated by logrank test. P value for (F) calculated by two-tailed Fisher's exact test. Error bars indicate mean ± SEM.

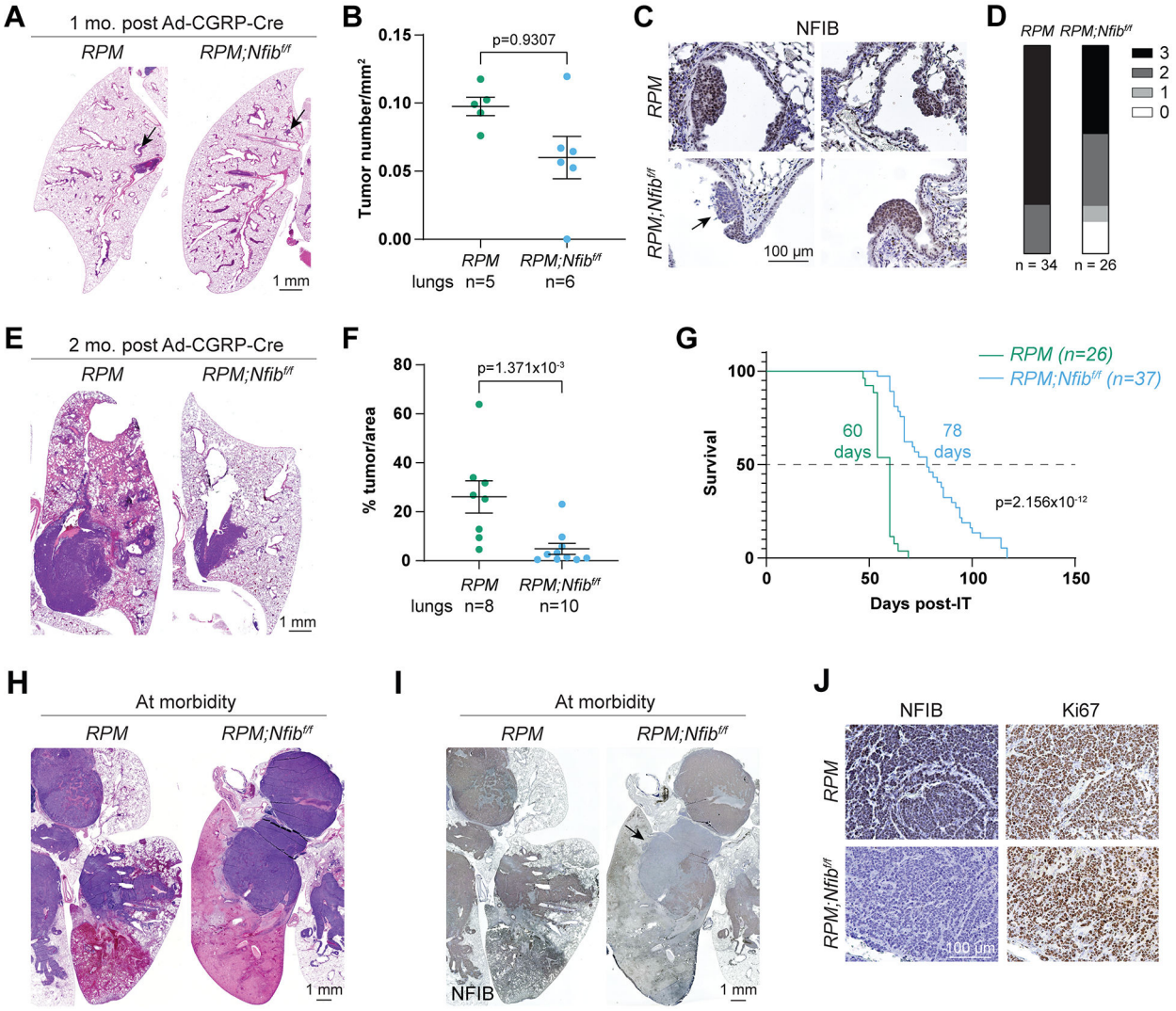

Fig. 3. NFIB loss is counterselected for at the time of tumor initiation in *RPM* mutant mice

A. Representative images of *RPM* and *RPM;Nfib*$^{f/f}$ mutant lungs stained with H&E, 1 month post Ad-CGRP-Cre infection. Arrows point to representative tumors. Scale bar, 1 mm. **B.** Quantification of (A) for tumor number per mm^2. **C.** Representative images of *RPM* and *RPM;Nfib*$^{f/f}$ mutant tumors immunostained for NFIB, 1 month post Ad-CGRP-Cre infection. The arrow points to a lesion with low/no NFIB expression. Scale bar, 100 μm. **D.** Staining intensity for NFIB expression from (C) from a scale of 0 (no signal) to 3 (high signal). **E.** Representative images of *RPM* and *RPM;Nfib*$^{f/f}$ mutant lungs stained with H&E, 2 months post Ad-CGRP-Cre infection. Scale bar, 1 mm. **F.** Quantification of (E) for tumor burden. **G.** Survival curves and median survival time of RPM and RPM;Nfibf/f mutant mice. **H.** Representative images of *RPM* and *RPM;Nfib*$^{f/f}$ mutant lungs stained with H&E at morbidity. Scale bar, 1 mm. **I.** Representative images of *RPM* and *RPM;Nfib*$^{f/f}$ mutant lungs immunostained for NFIB at morbidity. The arrow points to a large tumor with low/no NFIB expression. Scale bar, 1 mm. **J.** Representative images of *RPM* and *RPM;Nfib*$^{f/f}$ mutant tumors immunostained for NFIB and Ki67. The near-ubiquitous staining for Ki67 made it

challenging to accurately quantify the number of positive cells. Scale bar, 100 μm. P values in (B) and (F) calculated by two tailed Mann-Whitney test. P value in (G) calculated by logrank test. Error bars indicate mean ± SEM.

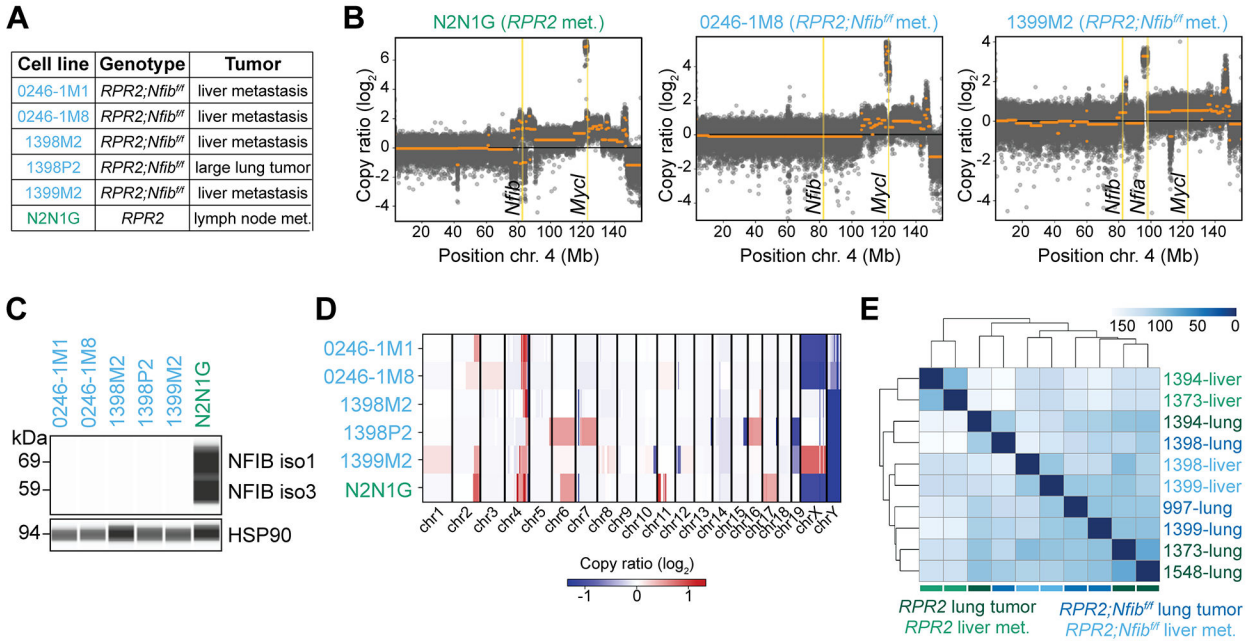

Fig. 4. NFIB^{neg} and NFIB^{high} SCLC metastases display distinct chromosomal and transcriptional features

A. Cell lines used for low-pass whole genome sequencing, their genotypes, and the type of tumor from which they were derived. **B.** Plots showing chromosome 4 gains and losses from three cell lines, as noted. Yellow lines indicate loci for *Nfib*, *Mycl*, and *Nfia* for 1399M2. N2N1G cells are derived from lymph node metastases from the *RPR2* model and show *Nfib* genomic amplification as well as *Mycl* amplification. Cell lines derived from liver metastases from the *RPR2;Nfib$^{f/f}$* model show no genomic amplification of the *Nfib* locus with the exception of 1399M2. **C.** Immunoassay for NFIB levels in cell lines in (A). Iso1 and iso3 indicate protein isoforms 1 and 3 of NFIB, respectively. HSP90 serves as a loading control. **D.** Plots showing genome-wide gains and losses from low-pass whole genome sequencing of cell lines in (A). Note the loss of chr19 in two of the *RPR2;Nfib$^{f/f}$* cell lines (1398M2 and 1399M2). **E.** Principal component analysis of RNA sequencing from primary lung tumors and liver metastases macrodissected from the *RPR2* and the *RPR2;Nfib$^{f/f}$* models. **F, G.** Top enriched terms from KEGG 2021 Human pathways in genes upregulated in liver metastases over primary lung tumors in the *RPR2* (F) and *RPR2;Nfib$^{f/f}$* (G) models. Differentially expressed genes (log2 fold change > 1.5, adjusted p value < 0.05) were filtered for those that did not overlap with the liver gene set in the Mouse Gene Atlas to

account for contaminating normal liver tissue. P values were calculated by Enrichr (Fisher's exact test).

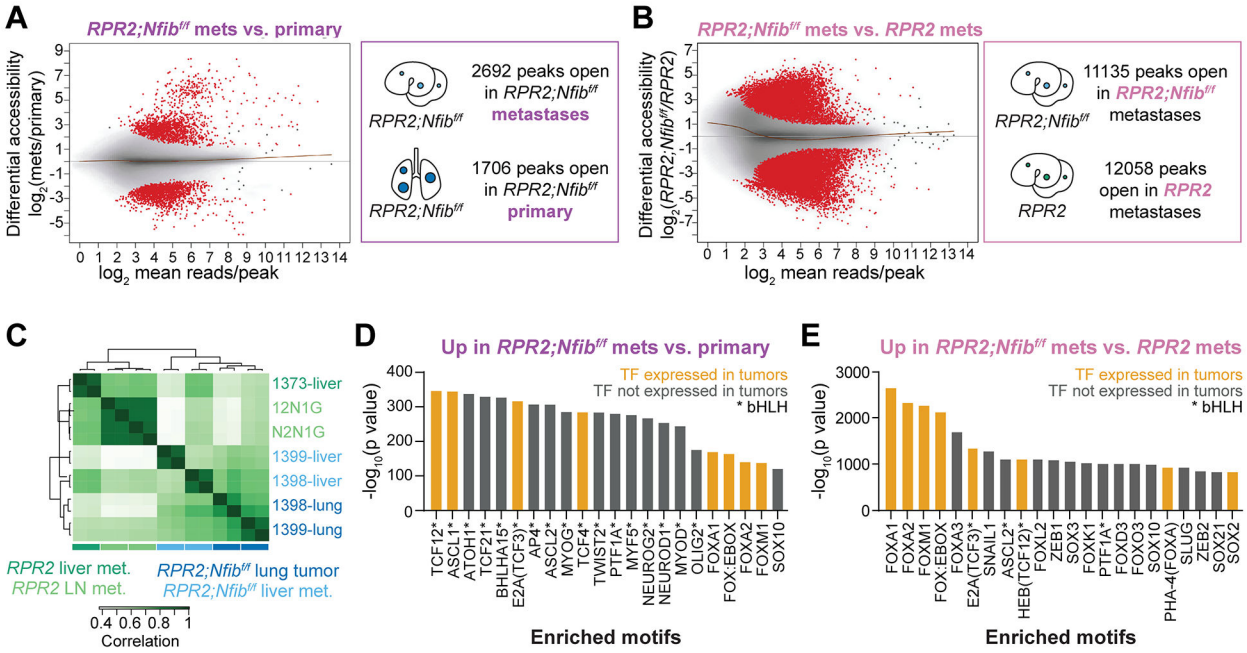

Fig. 5. NFIB^{neg} SCLC metastases show distinct chromatin states enriched for FOXA1/2 and ASCL1-related motifs

A, B. Differential accessibility (log2 fold change in reads per peak) plotted against the mean reads per peak by ATAC sequencing. Comparisons are between cell lines derived from *RPR2;Nfib$^{f/f}$* mutant metastases (mets) and cell lines derived from (A) *RPR2;Nfib$^{f/f}$* mutant primary tumors and (B) *RPR2* mutant metastases. Number of peaks that are differentially accessible are indicated. **C.** Correlation of ATAC sequencing with cell lines derived from *RPR2;Nfib$^{f/f}$* mutant liver metastases, *RPR2;Nfib$^{f/f}$* mutant primary lung tumors, *RPR2* mutant liver metastases, and *RPR2* mutant lymph node (LN) metastases. **D, E.** Motif enrichment in regions differentially open in *RPR2;Nfib$^{f/f}$* metastases from (A) and (B), respectively. Orange bars indicate motifs for transcription factors that are expressed in SCLC tumors as determined by RNA sequencing (see Figure S6C). Asterisks indicate basic helix-loop-helix (bHLH) transcription factors. Duplicate motifs identified for TCF12 (C), TCF3 (D), and FOXA1 (C,D) are not shown but can be found in Table S5.

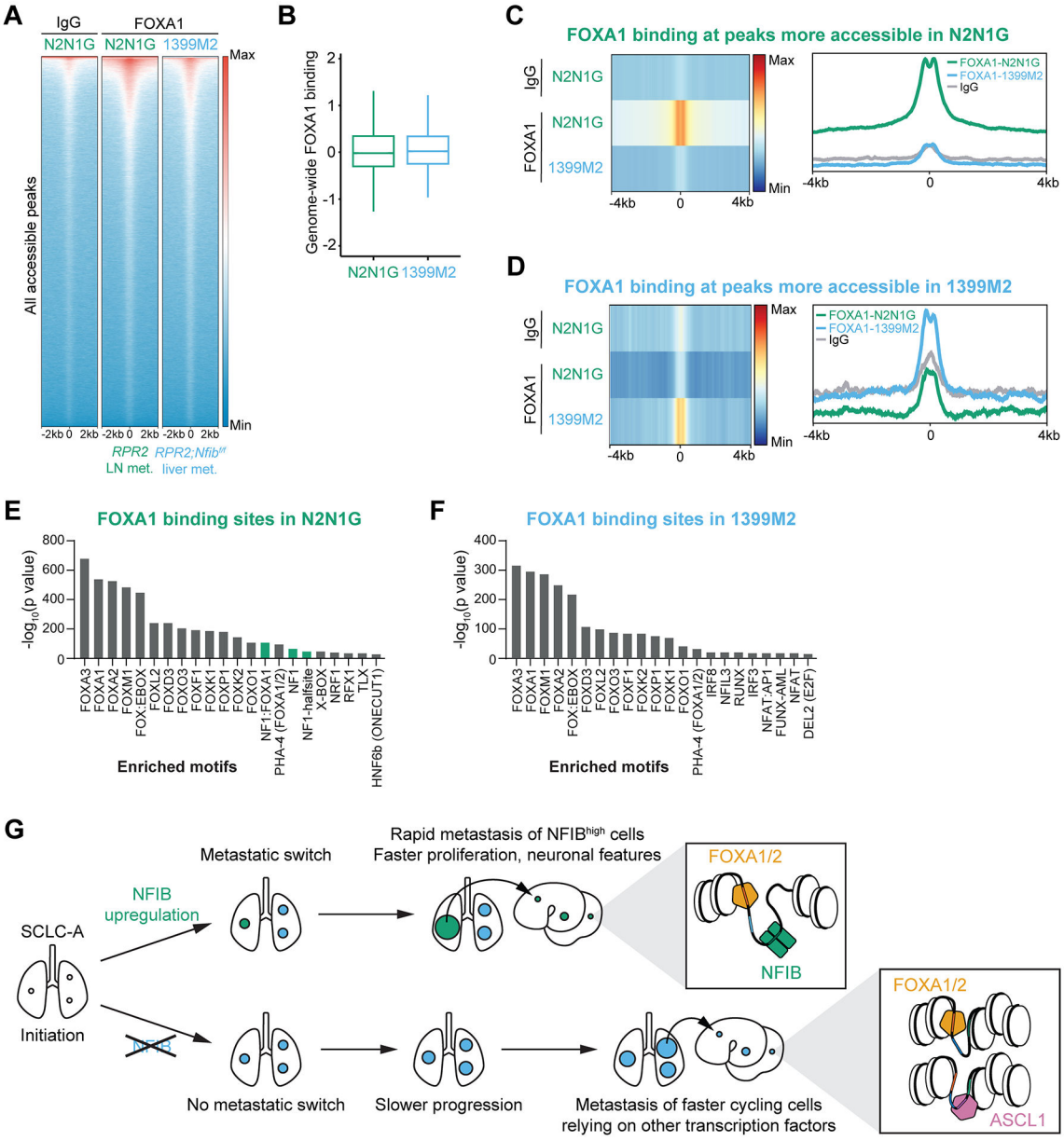

Fig. 6. FOXA1 binding sites are enriched in open chromatin regions in NFIB^{neg} SCLC cells

A. Tornado plot showing IgG and FOXA1 binding signal by CUT&RUN analysis at all accessible ATAC peaks in N2N1G (NFIB^{high} cell line derived from *RPR2* metastasis) and 1399M2 (NFIB^{neg} cell line derived from *RPR2;Nfib$^{f/f}$* metastasis). **B.** Quantitation of genome-wide FOXA1 binding in (A) shows no significant difference between N2N1G and 1399M2. **C, D.** Heatmap and profile plots showing FOXA1 binding at ATAC peaks that lose (C) and gain (D) accessibility in 1399M2 compared to N2N1G. **E, F.** Motif enrichment in FOXA1 binding sites in N2N1G (E) and 1399M2 (F). Green bars in (E) indicate motifs for NFI family members. Duplicate motifs for FOXA1 and motifs for transcription factors without mouse orthologs are not shown but can be found in Table S6. **G.** Model for metastasis of SCLC-A tumors. When SCLC cells can upregulate NFIB

(top), high NFIB activity acts as a switch that promotes tumor growth and metastasis. NFIB upregulation opens the chromatin at numerous loci in the genome, with FOXA1/2 as possible co-factors. When SCLC cells are unable to upregulate NFIB (bottom, for example when the gene is knocked out), tumor progression is slower, and cells that metastasize may rely on transcription factors such as ASCL1 and FOXA1/2, which may work in independent programs.